Anaerobic oxidation of methane alters sediment records of sulfur, iron and phosphorus in the Black Sea

Matthias Egger[1], Peter Kraal[1], Tom Jilbert[1,2], Fatimah Sulu-Gambari[1], Célia J. Sapart[3,4], Thomas Röckmann[3] and Caroline P. Slomp[1]

[1]Department of Earth Sciences – Geochemistry, Faculty of Geosciences, Utrecht University, P.O. Box 80021, 3508 TA, Utrecht, The Netherlands
[2]Now at: Department of Environmental Sciences, Faculty of Biological and Environmental Sciences, University of Helsinki, P.O. Box 65 (Viikinkaari 2a), 00014 Helsinki, Finland
[3]Institute for Marine and Atmospheric Research Utrecht (IMAU), Utrecht University, Princetonplein 5, 3584 CC Utrecht, The Netherlands
[4]Laboratoire de Glaciologie, Université Libre de Bruxelles, Belgium

Correspondence to: Matthias Egger (m.j.egger@uu.nl)

Abstract. The surface sediments in the Black Sea are underlain by extensive deposits of iron (Fe) oxide-rich lake sediments that were deposited prior to the inflow of marine Mediterranean Sea waters ca. 9000 years ago. The subsequent downward diffusion of marine sulfate into the methane-bearing lake sediments has led to a multitude of diagenetic reactions in the sulfate-methane transition zone (SMTZ), including anaerobic oxidation of methane (AOM) with sulfate. While the sedimentary cycles of sulfur (S), methane and Fe in the SMTZ have been extensively studied, relatively little is known about the diagenetic alterations of the sediment record occurring below the SMTZ. Here we combine detailed geochemical analyses of the sediment and pore water with multicomponent diagenetic modeling to study the diagenetic alterations below the SMTZ at two sites in the western Black Sea. We focus on the dynamics of Fe, S and phosphorus (P) and demonstrate that diagenesis has strongly overprinted the sedimentary burial records of these elements. In line with previous studies in the Black Sea, we show that sulfate-mediated AOM substantially enhances the downward diffusive flux of sulfide into the deep limnic deposits. During this downward sulfidization, Fe oxides, Fe carbonates and Fe phosphates (e.g. vivianite) are converted to sulfide phases, leading to an enrichment in solid phase S and the release of phosphate to the pore water. Below the sulfidization front, high concentrations of dissolved ferrous Fe (Fe^{2+}) lead to sequestration of downward diffusing phosphate as authigenic vivianite, resulting in a transient accumulation of total P directly below the sulfidization front.

Our model results further demonstrate that downward migrating sulfide becomes partly re-oxidized to sulfate due to reactions with oxidized Fe minerals, fueling a cryptic S cycle and thus stimulating slow rates of sulfate-driven AOM ($\sim$ 1 - 5 pmol cm^{-3} d^{-1}) in the sulfate-depleted limnic deposits. However, this process is unlikely to explain the observed release of dissolved Fe^{2+} below the SMTZ. Instead, we suggest that besides organoclastic Fe oxide reduction and reactivation of less reactive Fe oxides by methanogens, AOM coupled to the reduction of Fe oxides may also provide a possible mechanism for the high concentrations of Fe^{2+} in the pore water at depth. Our results reveal that methane plays a key role in the diagenetic alterations of Fe, S and P records in Black Sea sediments. The downward sulfidization into the limnic deposits is enhanced through sulfate-driven AOM with sulfate and AOM with Fe oxides may provide a deep source of dissolved Fe^{2+} that drives the sequestration of P in vivianite below the sulfidization front.

1   Introduction

Anaerobic oxidation of methane (AOM), a process initially regarded as a biogeochemical curiosity, functions as an important sink for oceanic methane (CH_4) by consuming > 90 % of all CH_4 produced in marine sediments (Knittel and Boetius, 2009; Reeburgh, 2007). Although recent studies indicate that the biological oxidation of CH_4 could be coupled to various additional electron acceptors such as nitrate and nitrite (Ettwig et al., 2010; Raghoebarsing et al., 2006) as well as metal oxides (Beal et al., 2009; Egger et al., 2015b; Riedinger et al., 2014; Scheller et al., 2016; Segarra et al., 2013; Sivan et al., 2011), sulfate (SO_4^{2-}) is commonly thought to be the dominant electron acceptor in anoxic marine systems (Knittel and Boetius, 2009; Reeburgh, 2007).

Nevertheless, a coupling between anaerobic CH_4 oxidation and iron (Fe) oxide reduction (Fe-AOM) could have a significant impact on sedimentary Fe cycling and related processes such as phosphorus (P) diagenesis, because of the 8:1 Fe-CH_4 stoichiometry of the reaction (Beal et al., 2009; Egger et al., 2015a; Rooze et al., 2016). Environmental conditions that favor Fe-AOM in marine systems are still poorly understood. The required co-occurrence of pore water CH_4 and abundant reducible Fe oxides suggests that Fe-AOM may occur in sediments that receive a relatively high input of Fe oxides compared to the in-situ production of sulfide, which could allow a portion of Fe oxides to escape the conversion to authigenic Fe sulfides and to remain preserved in the methanogenic sediments below the zone of SO_4^{2-} reduction (Egger et al., 2015b; Riedinger et al., 2014; Rooze et al., 2016). In addition, perturbations inducing transient diagenesis such as anthropogenic eutrophication or climate change may also create diagenetic environments that are likely favorable for Fe-AOM, as they provide a mechanism for the burial of Fe oxide-rich deposits below sulfidic sediment layers (Egger et al., 2015b; Riedinger et al., 2014).

The Black Sea represents a good example of a sedimentary system in which transient diagenesis associated with postglacial sea-level rise has led to the accumulation of sulfidic sediments above Fe oxide-rich deposits. Here, the establishment of a connection to the Mediterranean Sea through the shallow Bosporus around 9000 years ago (Degens and Ross, 1974; Soulet et al., 2011) led to the inflow of marine waters into a freshwater basin, resulting in permanent salinity/density stratification and in the development of euxinic conditions (i.e. free dissolved sulfide present in the bottom water), making the current Black Sea the largest permanently anoxic basin on Earth.

In the absence of oxygen and metal oxides, SO_4^{2-} reduction is the dominant benthic mineralization process of organic matter in Black Sea surface sediments below the chemocline (~ 100 m depth) (Jørgensen et al., 2001; Thamdrup et al., 2000). At present, SO_4^{2-} penetrates through the modern coccolith ooze (Unit I) and the marine sapropel (Unit II) sediments and a few meters into the Upper Pleistocene freshwater deposits (Unit III) (Arthur and Dean, 1998; Degens and Ross, 1974; Jørgensen et al., 2004). Below the SO_4^{2-}-bearing zone, methanogenesis takes over as the dominant process of organic matter degradation, resulting in the buildup of CH_4 in the pore water at depth.

Interactions between the cycles of sulfur (S) and CH_4 in Black Sea sediments have been extensively studied during recent years (Holmkvist et al., 2011b; Jørgensen et al., 2001, 2004; Knab et al., 2009; Leloup et al., 2007) and AOM coupled to SO_4^{2-} reduction (SO_4-AOM) was found to account for an estimated 7-18 % of total SO_4^{2-} reduction in these sediments (Jørgensen et al., 2001). The production of sulfide in the sulfate-methane transition zone (SMTZ) as a result of SO_4-AOM represents the main source of pore water sulfide at depth in the sediment. This intensified production of sulfide drives an enhanced downward diffusive flux of sulfide into the deep limnic deposits of Unit III,

2

75 forming a distinct diagenetic sulfidization front recognized as a black band or a series of bands owing to the
76 conversion of Fe oxides to Fe sulfides (Berner, 1974; Jørgensen et al., 2004; Neretin et al., 2004).

77 At present, the impact of the downward-migrating sulfidization front on sedimentary P, a key nutrient for marine
78 phytoplankton, and the potential role of Fe-mediated AOM in the deep limnic deposits remain largely unknown. A
79 buildup of ferrous Fe (Fe^{2+}) in the pore water at depth as found in previous studies (Holmkvist et al., 2011b;
80 Jørgensen et al., 2004; Knab et al., 2009), could indicate ongoing Fe reduction in the CH_4-bearing deep limnic
81 sediments and thus a potential coupling between AOM and Fe oxide reduction. The sediment records investigated up
82 to now, however, do not extend deep enough to allow the sedimentary cycling of Fe and related biogeochemical
83 processes below the sulfidization front to be investigated. In particular, the presence of abundant dissolved Fe^{2+}
84 combined with a potential release of pore water phosphate (HPO_4^{2-}) during reductive dissolution of Fe oxides may be
85 conducive to the formation of reduced Fe(II)-P minerals such as vivianite ($Fe_3(PO_4)_2*8H_2O$) below the sulfidization
86 front (Egger et al., 2015a; Hsu et al., 2014; März et al., 2008; Sivan et al., 2011). Post-depositional diagenetic
87 alterations as a result of downward sulfidization could therefore overprint burial records of P in the Upper
88 Pleistocene deposits.

89 In this study, we combine detailed geochemical analyses of the sediment and pore water with multicomponent
90 diagenetic modeling to study the diagenetic alterations below the lake-marine transition at two sites in the western
91 Black Sea. Focusing on the dynamics of S, Fe and P, we demonstrate that AOM coupled to SO_4^{2-} reduction enhances
92 the downward sulfidization and associated dissolution of Fe oxides, Fe carbonates and vivianite, supporting earlier
93 findings of an SO_4-AOM enhanced downward sulfidization in Black Sea sediments (Jørgensen et al., 2001). Below
94 the sulfidization front, downward diffusing HPO_4^{2-} precipitates as vivianite by reaction with the abundant dissolved
95 Fe^{2+}. We propose that organoclastic Fe oxide reduction, reactivation of less reactive Fe oxides by methanogens
96 (Sivan et al., 2016) and/or AOM coupled to the reduction of Fe oxides are the key processes explaining the high
97 concentrations of dissolved Fe^{2+} at depth in the sediment. Trends in total S and P with depth are significantly altered
98 by the above-mentioned reactions, highlighting that diagenesis may strongly overprint burial records of these
99 elements below a lake-marine transition.

100 **2   Materials and methods**

101 **2.1   Sample collection**

102 **2.1.1   Gravity core sampling**

103 Sediment samples were taken at two slope sites in the western Black Sea during a cruise in June 2013 with R/V
104 Pelagia. Gravity cores containing ~ 7 m of sediment were collected at sites 4 (43°40.6' N, 30°7.5' E; 377 meters
105 below sea surface (mbss)) and 5 (43°42.6' N, 30°6.1' E; 178 mbss) (Fig. 1), both situated below the current
106 chemocline (~ 100 m water depth). The core liners were pre-drilled with 2 cm diameter holes in two rows of 10 cm
107 resolution on opposing sides of the tube, offset by 5 cm and taped prior to coring. Upon recovery, the liners were cut
108 into 1 m sections, transferred to a temperature-controlled container set at in-situ bottom water temperature (11 °C)

3

109   and secured vertically. Subsequently, the taped holes were cut open and a cut-off syringe was inserted horizontally
110   directly after opening each hole.

111   From one series of holes, 10 mL of wet sediment was extracted at 20 cm resolution and immediately transferred into
112   a 65 mL glass bottle filled with saturated NaCl solution for CH_4 analysis. The NaCl solution was topped up after
113   addition of the sample, ensuring that no air bubbles remained. Each bottle was sealed with a black rubber stopper and
114   a screw cap and was subsequently stored upside-down at room temperature. From the second series of holes, 20 mL
115   sediment was extracted at 20 cm resolution, sealed with parafilm that was tightly closed with an elastic band, and
116   directly inserted into a nitrogen (N_2)-purged glove box. Subsequently, the sediment was transferred into a 50 mL
117   centrifuge tube and centrifuged (4500 rpm; 30 min). The supernatant from each centrifuged sample was filtered
118   through 0.45 µm pore size disposable filters via 20 mL plastic syringes in the glove box and collected in 15 mL
119   centrifuge tubes. The sediment fraction was stored frozen (-20 °C) for solid phase analysis. Filtered pore water
120   samples were sub-sampled under N_2 for analysis of dissolved HPO_4^{2-}, ammonium (NH_4^+), dissolved inorganic
121   carbon (DIC), Fe, manganese (Mn), SO_4^{2-} and sulfide ($\sum H_2S = H_2S + HS^-$) (see section 2.2) Additional samples of 10
122   mL of sediment were collected at approximately 50 cm resolution and transferred into pre-weighed 15 mL glass vials
123   to determine porosity from gravimetric water loss.

2.1.2   Multicore sampling

125   To sample the surface sediment, sediment cores (30-60 cm of sediment and at least 10 cm of overlying water) were
126   recovered using an octopus multicorer (core diameter 10 cm). After recovery, the cores were stoppered at the base
127   and at the top and immediately transported to a temperature-controlled container (11 °C). One multicore from each
128   cast was pre-drilled with 2 cm diameter holes in two rows at 10 cm resolution on opposing sides of the tube, offset
129   by 5 cm, and taped prior to coring. These holes were sampled for CH_4 as described for the gravity cores. Another
130   core was directly inserted into a N_2-purged glove box through an airtight hole in the base. A bottom water sample
131   was collected using a 20 mL plastic syringe and the remaining bottom water was removed with a Tygon tube.
132   Subsequently, the core was sliced anoxically with decreasing resolution at depth, i.e. 0.5 cm resolution for the first 0-
133   2 cm, 1 cm resolution between 2-10 cm, 2 cm resolution between 10-20 cm and 4 cm resolution for the rest of the
134   core (> 20 cm). For each slice a sub-sample was placed in a pre-weighed 15 mL glass vial for water content and solid
135   phase analysis and stored under N_2 in airtight jars at -20 °C. A second sub-sample was transferred to a 50 mL
136   centrifuge tube and centrifuged (4500 rpm; 30 min). Both the supernatant water from each centrifuged sample and
137   the bottom water sample were subsequently processed as described for the gravity cores.
138   Visual alignment of the pore water profiles from the multicores with those of the gravity cores showed that the first ~
139   20 to 30 cm of sediment was lost during long coring. At site 5, the sediment in the multicore consisted of a gray and
140   homogeneous turbidite below 1.5 cm depth. The depth for the gravity core at site 5 was thus corrected for the loss of
141   the marine deposits, which were previously reported to be about 50 cm thick at a site in close proximity to site 5
142   (43°42.63' N, 30°6.12' E; 181 mbss) (Jørgensen et al., 2004)

4

2.2 Pore water subsampling

A sub-sample of 0.5 mL was immediately transferred into a glass vial containing 1.5 mL of 8 M NaOH solution for analysis of dissolved sulfide. Sub-samples for total dissolved Fe and Mn, which are assumed to represent Fe(II) and Mn(II), were acidified with 10 μL 35 % suprapur HCl per mL of sub-sample. Note, however, that the dissolved (< 0.45 μm) Fe and Mn pools likely consist of a mixture of truly dissolved (aqueous), as well as organically complexed, colloidal and nanoparticulate Fe and Mn species (Raiswell and Canfield, 2012). Another 1 mL of pore water for HPO_4^{2-} analysis was acidified with 4 μL 5 M HCl. Pore water SO_4^{2-} was analyzed with ion chromatography (IC) in a 10-fold diluted sample (0.15 mL of pore water with 1.35 mL of de-oxygenated UHQ water). Sub-samples for DIC analysis (0.5 mL) were collected in glass vials (4.9 mL) to which 4.4 mL of 25 g/L NaCl solution was added, making sure that no headspace remained. Aliquots of the remaining pore water were used for the measurement of alkalinity (determined onboard by titrating 1 mL of untreated sub-sample with 0.01 M HCl; results presented in the Supplementary Information only) and NH_4^+. All sub-samples were stored at 4 °C and brought to room temperature just before analysis. Subsampling for sulfide was performed immediately after filtration and all other subsampling was performed within 4 hours of core recovery.

Pore water sub-samples for HPO_4^{2-}, DIC and sulfide were directly analyzed colorimetrically onboard on two separate QuAAtro (SEAL Analytical, Germany) auto analyzers. HPO_4^{2-} was measured at 880 nm after the formation of molybdophosphate-complexes (Murphy and Riley, 1962). Samples for DIC were acidified online after being oxidized by H_2O_2 and analyzed as described by Stoll et al. (2001). To keep the dissolved sulfide in the non-volatile HS^- form under alkaline conditions, 1.5 mL of 8 mM NaOH was added to the sulfide samples, which were subsequently analyzed using the methylene blue method as described by Grasshoff (1969). Sub-samples for dissolved Fe and Mn were analyzed onshore by ICP-OES (Perkin Elmer Optima 3000 Inductively Coupled Plasma - Optimal Emission Spectroscopy). For the analysis of pore water CH_4, a volume of 10 mL N_2 was injected into the CH_4 serum flasks (while a needle inserted through the septum allowed 10 mL of water to escape) to create a headspace from which a subsample was collected with a gas-tight syringe. Subsequently, CH_4 concentrations were determined in the home laboratory after injection into a Thermo Finnigan Trace GC gas chromatograph (Flame Ionization Detector). $\delta^{13}C$-CH_4 and δD-CH_4 (D, deuterium) were analyzed by Continuous Flow Isotope Ratio Mass Spectrometry (CF-IRMS) as described in detail in (Brass and Röckmann, 2010) and (Sapart et al., 2011).

2.3 Bulk sediment analysis

Sediment samples were freeze-dried, powdered and ground in an agate mortar in an argon (Ar)-filled glove box and split into oxic and anoxic fractions. Samples from the oxic fraction were used for total elemental and organic carbon (C_{org}) analyses under normal atmospheric conditions, whereas anoxic splits for sediment P and Fe speciation were kept under an inert, oxygen-free Ar or N_2 atmosphere at all times to avoid oxidation artefacts (Kraal and Slomp, 2014; Kraal et al., 2009).

2.3.1 Total elemental composition and organic carbon

A split of ~ 125 mg of freeze-dried sediment was dissolved overnight in 2.5 mL HF (40 %) and 2.5 mL of $HClO_4/HNO_3$ mixture, in a closed Teflon bomb at 90 °C. The acids were then evaporated at 160 °C and the resulting gel was dissolved overnight in 1 M HNO_3 at 90 °C. Total elemental concentrations in the 1 M HNO_3 solutions were determined by ICP-OES. A second split of 0.3 g freeze-dried sediment was used to determine the C_{org} content using an elemental analyzer (Fison Instruments model NA 1500 NCS) after carbonate removal from the sediment with two washes with 1 M HCl (4 h and 12 h) followed by two washes with UHQ water and subsequent drying of the samples (Van Santvoort et al., 2002).

2.3.2 Sediment P fractionation

To determine the solid phase partitioning of P, aliquots of 0.1 g dried sediment were subjected to the SEDEX sequential extraction procedure after Ruttenberg (1992), as modified by Slomp et al. (1996b), but including the first $MgCl_2$ step (Table 1). Sediment P was fractionated as follows: i) exchangeable-P ("P_{exch}", extracted by 1 M $MgCl_2$, pH 8, 0.5 h), ii) Fe-associated P ("P_{Fe}", extracted by citrate-bicarbonate-dithionite (CDB), buffered to pH 7.5 with Na citrate/Na bicarbonate, 8 h, followed by 1 M $MgCl_2$, pH 8, 0.5 h), iii) authigenic Ca-P ("$P_{authi\ Ca-P}$", including carbonate fluorapatite, biogenic hydroxyapatite and $CaCO_3$-bound P, extracted by 1 M Na acetate solution, buffered to pH 4 with acetic acid, 6 h, followed by 1 M $MgCl_2$, pH 8, 0.5 h), iv) detrital Ca-P ("P_{detr}", extracted by 1 M HCl, 24 h) and v) organic P ("P_{org}", after ashing at 550 °C for 2 h, extracted by 1 M HCl, 24 h). The $MgCl_2$ washes in steps ii and iii were to ensure that any HPO_4^{2-} re-adsorbed during CDB or acetate extraction was removed and included in the pools of Fe-associated P and authigenic Ca-P, respectively. Sediments were shielded from oxygen inside an Ar-filled glovebox until step 3 of the SEDEX procedure to eliminate the potential conversion of Ca-P to Fe-bound P due to pyrite oxidation upon oxygen exposure (Kraal and Slomp, 2014; Kraal et al., 2009). Dissolved HPO_4^{2-} in the CDB solution was analyzed by ICP-OES. For all other solutions, HPO_4^{2-} was determined colorimetrically (Strickland and Parsons, 1972) on a Shimadzu spectrophotometer using the ammonium heptamolybdate – ascorbic acid method.

2.3.3 Sediment Fe fractionation

Sediment Fe was fractionated into i) carbonate associated Fe ("Fe_{carb}", including siderite and ankerite, extracted by 1 M Na-acetate brought to pH 4.5 with acetic acid, 24 h), ii) easily reducible (amorphous) oxides ("Fe_{ox1}", including ferrihydrite and lepidocrocite, extracted by 1 M hydroxylamine-HCl, 24 h), iii) reducible (crystalline) oxides ("Fe_{ox2}", including goethite, hematite and akagenéite, extracted by Na-dithionite buffer, pH 4.8, 2 h) and iv) Fe in recalcitrant oxides (mostly magnetite, "Fe_{mag}", extracted by 0.2 M ammonium oxalate / 0.17 M oxalic acid solution, 2 h), according to Poulton and Canfield (2005), using a 50 mg aliquot of dried sediment (Table 1). An additional aliquot of 50 mg was subjected to an adapted sequential extraction procedure after Claff et al. (2010), separating labile Fe(II) ("$Fe(II)_{HCl}$") and Fe(III) ("$Fe(III)_{HCl}$") using 1 M HCl (4 h) from crystalline Fe oxide minerals ("$Fe(II)_{CDB}$", Na-dithionite buffer, pH 4.8, 4 h) and from pyrite ("Fe_{pyrite}", concentrated nitric acid, 2 h), for all multicores as well as for the long core at site 4 (Table 1).

6

211 At site 4 (multicore only) and 5 (multicore and gravity core), aliquots of 0.5 g dried sediment were used to
212 sequentially determine the amount of FeS (acid volatile sulfur, "AVS", using 6 M HCl) and FeS_2 (chromium
213 reducible sulfur, "CRS", using acidic chromous chloride solution) via the passive diffusion method described by
214 (Burton et al., 2008) using iodometric titration of the ZnS formed in the alkaline Zn acetate traps to quantify AVS
215 and CRS (Table 1).

216 **2.4   Diagenetic model**

217 **2.4.1   General form**

218 A multicomponent transient diagenetic model was developed for site 4 based on existing diagenetic models (Reed et
219 al., 2011a, 2011b; Rooze et al., 2016) to gain a better understanding of the transient diagenesis in Black Sea
220 sediments and to investigate the potential for Fe-AOM as a source of pore water Fe^{2+} at depth. The model describes
221 the cycling of dissolved and particulate chemical species in a 1D sediment column (Berner, 1980). A total of 25
222 different chemical species (Table 2) were subjected to a suite of biogeochemical reactions (Table 3) and vertical
223 transport through burial, as well as molecular diffusion for dissolved species (Boudreau, 1997; Soetaert et al., 1996;
224 Wang and Van Cappellen, 1996). The general diagenetic equations for solid (Eq. (1)) and dissolved species (Eq. (2))
225 are, respectively,

226    $(1 - \phi)\frac{\partial C_S}{\partial t} = -(1 - \phi)v\frac{\partial C_S}{\partial x} + \sum R_S$ (1)

227    $\phi\frac{\partial C_{aq}}{\partial t} = \phi D'\frac{\partial^2 C_{aq}}{\partial x^2} - \phi u\frac{\partial C_{aq}}{\partial x} + \sum R_{aq}$ (2)

228 where C_S is the concentration of the solid species (mol L^{-1}; mass per unit volume of solids), C_{aq} the concentration of
229 the dissolved species (mol L^{-1}; mass per unit volume of pore water), t is time (yr), ϕ the sediment porosity, x the
230 distance from the sediment-water interface (cm), D' the diffusion coefficients of dissolved species in the sediment
231 (cm^2 yr^{-1}) adjusted for the considered setting (Supplementary Table S1) (Boudreau, 1997) and corrected for the
232 tortuosity in the porous medium (Boudreau, 1996) (see Supplementary Information). $\sum R_S$ and $\sum R_{aq}$ are the net
233 reaction rates of the solid and dissolved species from the chemical reactions they participate in (Table 3), and v and
234 u the advective velocities (cm yr^{-1}) of the solid and the dissolved species, respectively. Porosity and advective
235 velocities were described by depth-dependent functions to account for sediment compaction (Meysman et al., 2005;
236 Reed et al., 2011a) (see Supplementary Information and Supplementary Fig. S1).
237 Reactions considered by the model and corresponding reaction equations are given in Tables 3 and 4, respectively,
238 and are divided into primary redox reactions and other biogeochemical reactions, including various mineral
239 formation and dissolution reactions (Reed et al., 2011a, 2011b; Rooze et al., 2016). Corresponding reaction
240 parameters were mostly taken from the literature or, if these were not available or no fit to the data could be obtained
241 with existing parameter ranges, constrained using the extensive geochemical dataset for site 4 (Table 5). A model
242 sensitivity analysis for key parameters is provided in the Supplementary Information (Supplementary Figs. S2 and
243 S3).
244 To account for differences in reactivity and crystallinity between different species, organic matter and Fe oxides are
245 divided into three different pools, representing highly reactive (α), less reactive (β) and non-reactive (i.e. inert) (γ)

7

246   phases. For the Fe oxides, only the α phase is used by organoclastic Fe reduction (Table 3), while the β phase is also

247   used by Fe-AOM. This assumption was made to test whether the pore water and sediment profiles observed in the

248   Black Sea can be reproduced with Fe-AOM as the main Fe reduction pathway at depth. In addition, it allows an

249   assessment of the potential impact of Fe-AOM on sedimentary CH_4 cycling. Note that, as a consequence of the

250   exclusion of organoclastic Fe reduction at depth, the model results should not be interpreted as proof for Fe-AOM

251   but rather imply that it is a possible mechanism.

252   The succession of oxidants during organic matter decomposition (Froelich et al., 1979) is described by means of

253   Monod kinetics (Table 4), whereby those oxidants with the highest metabolic free energy yield are used

254   preferentially until they become limiting and the oxidant with the next highest energy yield is used (Berg et al., 2003;

255   Boudreau, 1996; Reed et al., 2011b; Rooze et al., 2016; Wang and Van Cappellen, 1996). Oxidants considered by the

256   model are (in descending order of energy yield) O_2, nitrate (NO_3^-), Fe oxides and SO_4^{2-}. Once these oxidants are

257   exhausted, organic matter remineralization occurs by methanogenesis. Corresponding limiting concentrations for the

258   oxidants are taken from (Reed et al., 2011a) (Table 5). In addition, an attenuation factor, Ψ, is used to slow down

259   anaerobic organic matter degradation through SO_4^{2-} reduction and methanogenesis, thus allowing for better

260   preservation of organic matter under anoxic bottom water conditions (Moodley et al., 2005; Reed et al., 2011a,

261   2011b).

262   Cycling of S is simulated using five different chemical species, i.e. Fe monosulfides (FeS), pyrite (FeS_2), elemental S

263   (S_0), dissolved sulfide and pore water SO_4^{2-} (Table 2), combined in a network of various biogeochemical reactions

264   (Table 3). The CH_4 cycle includes CH_4 production from organic matter and from DIC (i.e. CO_2), as well as CH_4

265   oxidation coupled to the reduction of O_2, SO_4^{2-} and $Fe(OH)_3$ (Table 3). For AOM a bimolecular rate equation was

266   used (Table 4), which is the most common way to parameterize AOM in reactive transport models (Regnier et al.,

267   2011) and allows the use of largely unknown half-saturation constants, in particular for the putative Fe-AOM

268   pathway, to be avoided. Although Mn-oxides have also been suggested to be a thermodynamically favorable electron

269   acceptor for AOM (Beal et al., 2009), they were not included in the model because of the relatively low Mn

270   concentrations (~ 15 μmol g^{-1} for total sedimentary Mn and < 30 μM for dissolved Mn^{2+}; Supplementary Fig. S2 and

271   S3) when compared to Fe and the likely presence of most of the Mn in the form of Mn-carbonates.

272   The P forms included in the model are pore water HPO_4^{2-}, authigenic Ca-P, organic P and detrital P, as well as Fe-

273   bound P, i.e. P associated with Fe oxides and P in vivianite (Table 2). The removal of dissolved Fe^{2+} through

274   formation of the Fe minerals FeS, siderite ($FeCO_3$) and vivianite is also included in the model (Table 3). Mass

275   balances for all chemical species included in the model are given in Supplementary Table S2.

276   The boundary conditions at the sediment surface were specified as time-dependent depositional fluxes for the

277   particulate components and as fixed bottom water concentrations for the dissolved species, while a zero gradient

278   boundary condition was set for all chemical species at the base of the model domain (Fig. 2 and Supplementary

279   Table S3). To avoid potential interferences of the lower boundary conditions with the model results in the upper

280   sediments (see Supplementary Fig. S6), the model depth was set to 3000 cm and divided into 500 grid cells. The

281   thickness of the upper layer was set at 1 cm, and the thickness of the following grid layers increased exponentially to

282   ~ 6 cm at 800 cm depth and to ~18 cm at 3000 cm depth. In this paper, only the upper 800 cm are shown. However,

283   all profiles extending over the full depth range are provided in the Supplementary Information file (Supplementary

8

284 Fig. S5 and Fig. S7). The model code was written in R using the marelac geochemical dataset package (Soetaert et

285 al., 2010) and the ReacTran package (Soetaert and Meysman, 2012) to calculate the transport in porous media. The

286 set of ordinary differential equations was subsequently solved numerically with the lsoda integrator algorithm

287 (Hindmarsh, 1983; Petzoldt, 1983)

2.4.2 Transient scenario

289 The model applied in this study simulates the sediment deposition during the last 25000 years. A constant mass

290 accumulation rate of 0.06 g cm^{-2} yr^{-1} over the Holocene was assumed. In order to reduce the computing time for the

291 freshwater period, a higher mass accumulation rate of 1 g cm^{-2} yr^{-1} was used between 25000 and 10000 years before

292 present (B.P.) and all fluxes were corrected accordingly (i.e. multiplied with a factor of 16.67). Inflow of

293 Mediterranean saltwater into the Black Sea basin was modelled assuming an initial salinity of 1 for the freshwater

294 lake and a linear increase to a salinity of 22 between 8500 and 1500 years B.P. (Fig. 2). Such a salinization scenario

295 results in a good fit to the chloride (Cl$^-$) profile (Fig. 3) and compares well with a previous salinity reconstruction

296 suggesting a linear increase in salinity of 1 to 22 between 9000 ± 500 years B.P. and 2000 ± 500 years B.P. (Soulet et

297 al., 2010). Bottom water salinity was converted to Cl$^-$ and SO$_4^{2-}$ using the molecular weights and seawater density

298 derived from the marelac geochemical dataset package (Soetaert et al., 2010) (Supplementary Table S1). A shift

299 from oxic towards euxinic conditions around 7600 years B.P., with a peak in organic matter loading around 5300

300 years B.P. and constant elevated organic matter fluxes after 2700 years B.P. was assumed, following a recent study

301 comprising data from seven sediment cores collected from the Black Sea (Eckert et al., 2013) (Fig. 2). In addition,

302 the input of organic matter was assumed to increase again in the last century, reflecting anthropogenic eutrophication

303 of waters on the adjacent continental shelf as previously reported (Capet et al., 2013; Kemp et al., 2009). With the

304 development of anoxic and sulfidic bottom-water conditions, depositional fluxes of reactive Fe oxides were assumed

305 to be zero (Fig. 2). In contrast, fluxes of Fe sulfides are high under euxinic conditions and dominated by FeS$_2$.

3 Results

3.1 Pore water profiles

308 Pore water profiles of SO$_4^{2-}$ show a linear decrease from $\sim$ 17 mM at the sediment water interface to a depth of $\sim$ 230

309 cm at both sites, below which CH$_4$ starts to accumulate in the pore water (Fig. 3). Bubble formation and degassing of

310 CH$_4$ during gravity coring could not be avoided because of the high concentrations of CH$_4$ in the limnic deposits

311 above the saturation of ca 1.3 mM CH$_4$ at atmospheric pressure (calculated for a salinity of 22 and a temperature of

312 25 °C using the algorithm from Mogollón et al. (2013)). Observations of increased outgassing with depth during

313 coring suggest that the low CH$_4$ concentrations in the deeper sediments at both sites are due to enhanced outgassing

314 with increasing levels of CH$_4$. Pore water profiles of NH$_4^+$ at both sites are similar and concentrations increase to $\sim$ 3

315 mM at depth, suggesting that actual CH$_4$ concentrations at both sites could be comparable. Most of the CH$_4$ values

316 thus only indicate the presence or absence of CH$_4$ and are not a quantitative measure (indicated as open diamonds in

317 Fig. 4). Note that the upper $\sim$ 300 cm of sediment at site 5 are likely less affected by CH$_4$ outgassing. Modeled pore

9

318 water concentrations of CH_4 on the other hand, show a steep increase below the SMTZ, comparable to the gradient

319 observed at site 5, and build up to concentrations of ~ 15 mM at depth (Supplementary Fig. S5).

320 The SMTZ is located around 230 cm depth in the sediment and is characterized by the removal of both pore water

321 SO_4^{2-} and dissolved CH_4. In this zone, SO_4-AOM drives the production of dissolved sulfide, DIC and alkalinity

322 (Supplementary Fig. S5) and diffusion of these pore water constituents away from the SMTZ (Fig. 3). Below the

323 sulfide diffusion front, Fe^{2+} accumulates in the pore water. Dissolved HPO_4^{2-} reaches a maximum around the depth

324 where sulfide levels drop below the detection limit of 1 μmol L^{-1}, followed by a steep decrease with depth.

325 Concentrations of pore water Mn^{2+} are more than an order of magnitude lower than those of dissolved Fe^{2+}, and

326 decrease from the sediment surface until ~ 200 cm depth, below which they slightly increase again (Supplementary

327 Fig. S5).

328 The smooth pore water profiles of $\delta^{13}C$-CH_4 and δD-CH_4 suggest that the isotopic composition of pore water CH_4

329 (available for site 5 only) is less affected by the CH_4 loss and reveals a biological origin in the limnic deposits, with

330 hydrogenotrophic carbonate reduction, i.e. microbial reduction of CO_2 to CH_4 as the main methanogenic pathway for

331 the range of CH_4 isotope ratios observed in these sediments (Fig. 4) (Whiticar, 1999). Upward diffusing CH_4 shows a

332 gradual depletion in $\delta^{13}C$-CH_4 from ~ -74 ‰ at depth to ~ -96 ‰ around the SMTZ, followed by subsequent

333 progressive ^{13}C enrichment towards the sediment surface. δD-CH_4 shows a small enrichment from -226 ‰ at depth

334 to ~ -208 ‰ at the SMTZ and a strong shift towards high δD-CH_4 values of up to ~ 113 ‰.

335 **3.2   Solid phase profiles**

336 A pronounced excursion in sedimentary C_{org} at site 4 in combination with a shift from gray clay deposits to micro-

337 laminated black sediments indicates that the lake-marine transition, i.e. the transition between the marine sapropel

338 Unit II and the deep limnic sediments of Unit III (Arthur and Dean, 1998; Degens and Ross, 1974), is located around

339 a sediment depth of ~ 90 cm at site 4 (Fig. 5). At site 5, Unit I and Unit II were lost due to a turbidite, explaining the

340 low concentrations of C_{org} in the upper sediments.

341 Concentrations of solid S increase with decreasing depth from 20 μmol g^{-1} below 300 cm (sulfidization front) to ~

342 400 μmol g^{-1} in the upper 100 cm at both sites and are dominated by FeS_2 (Fig. 5). Iron oxides show a decrease from

343 ~ 100 μmol g^{-1} at depth to ~ 50 μmol g^{-1} in the sediments between 100 – 300 cm and a further decrease to ~ 10 μmol

344 g^{-1} closer to the sediment surface. Amorphous Fe oxides (Fe_{ox1}) and more crystalline oxides (Fe_{ox2}) both account for

345 half the total amount of Fe oxides, with a small contribution of recalcitrant oxides (Fe_{mag}) (Supplementary Fig. S4).

346 The results from the two different Fe extractions applied in this study (Table 1) generally compare well

347 (Supplementary Fig. S4). Note, however, that the Fe oxides in Fig. 5 represent the results from the extraction after

348 Poulton and Canfield (2005). Results from the Fe extractions modified from Claff et al. (2010) are provided in the

349 Supplementary Information only. Sedimentary Mn content is relatively low at all three sites, ranging from ~ 5-10

350 μmol g^{-1} in the marine sediments to ~ 15 μmol g^{-1} in the deep limnic deposits of Unit III (Supplementary Fig. S4).

351 Sediments below the sulfidization front are characterized by high Fe carbonate contents of ~ 100 μmol g^{-1}. The sharp

352 depletion in Fe carbonate around the sulfidization front could only be reproduced in the model by assuming Fe

10

353   carbonate dissolution by dissolved sulfide (Table 3). These results suggest a conversion of reactive Fe from

354   carbonate toward sulfide phases in the presence of abundant dissolved sulfide.

355   Units I and II show high concentrations of organic P, which accounts for ~ 30 % of total P in these sediments (Fig.

356   5). Low organic P and high concentrations of detrital P in the upper sediments at site 5 are due to the turbidite. The

357   limnic deposits of Unit III are generally depleted in organic P (< 6 % of total P) and enriched in detrital P.

358   Authigenic Ca-P shows little variation in the sediments of Unit III, accounting for ~ 20 to 30 % of total P at the two

359   sites. The contribution of Fe-associated P, on the other hand, is reduced in the limnic deposits of Unit III exposed to

360   the downward diffusing sulfide (~ 20 %) when compared to the sediments below the sulfidization front (~ 30 %).

361   Concentrations of exchangeable P are < 2 μmol g^{-1} for sediments above the SMTZ and < 1 μmol g^{-1} for sediments at

362   depth (data not shown).

363   Modeled SO_4^{2-} reduction rates show two distinct peaks of ~ 200 pmol SO_4^{2-} cm^{-3} d^{-1} in the sediments of Unit II and

364   in the sediments around the SMTZ (Fig. 6). Rates of CH_4 production are highest (~ 30 pmol CH_4 cm^{-3} d^{-1}) in the

365   organic-rich marine deposits of Unit II and in the limnic deposits below the SMTZ. The sediments around the SMTZ

366   are further characterized by high rates of SO_4-AOM (~ 200 pmol cm^{-3} d^{-1}), whereas sediments directly below the

367   sulfidization front show enhanced rates of S_0 disproportionation (~ 15 pmol cm^{-3} d^{-1}). Organoclastic SO_4^{2-} reduction

368   provides the main source for pore water sulfide in the organic-rich marine deposits, while SO_4-AOM and S_0

369   disproportionation are the dominant sources of dissolved sulfide in sediments around the SMTZ and directly below

370   the sulfidization front, respectively. Rates of Fe-AOM are generally low (< 0.04 pmol CH_4 cm^{-3} d^{-1}) and restricted to

371   the limnic deposits only.

372   **3.3   Temporal evolution**

373   The temporal evolution in pore water and solid phase constituents illustrates the impact of the lake-marine transition

374   on the sediment geochemistry (Fig. 7). Concentrations of pore water Cl$^-$ and SO_4^{2-} increase with the intrusion of

375   marine Mediterranean Sea waters, accompanied by a decrease in dissolved CH_4 and accumulation of pore water

376   sulfide in the shallower sediments. Dissolved Fe^{2+} becomes restricted to non-sulfidic pore waters at depth, while

377   HPO_4^{2-} and solid S start to accumulate in the presence of dissolved sulfide. Iron oxides decrease in the surface

378   sediments as well as in the sediments at depth. Vivianite, on the other hand, becomes increasingly enriched in

379   sediments below the downward diffusing sulfide front.

380   **4.   Discussion**

381   **4.1 Coupled S, CH_4 and Fe dynamics**

382   **4.1.1 Organoclastic SO_4^{2-} reduction**

383   Model-derived areal rates of total SO_4^{2-} reduction of ~ 0.24 mmol SO_4^{2-} m^{-2} d^{-1} (Table 6), i.e. the total amount of

384   SO_4^{2-} reduced per square meter of sea floor, compare well with calculated diffusive fluxes of SO_4^{2-} into the sediment

385   at sites 4 and 5 (~ 0.21 and 0.20 mmol SO_4^{2-} m^{-2} d^{-1}, respectively) and are in good agreement with previous SO_4^{2-} flux

386   estimates of 0.17 to 0.28 mmol SO_4^{2-} m^{-2} d^{-1} for sediments of the western Black Sea (Jørgensen et al., 2001). In the

11

387   model, organoclastic SO_4^{2-} reduction accounts for > 65 % of total organic matter degradation in the upper 800 cm of
388   sediment, supporting previous conclusions that SO_4^{2-} reduction represents the dominant mineralization process of
389   organic matter in sediments below the chemocline (Jørgensen et al., 2001; Thamdrup et al., 2000). The remaining <
390   25 % of organic matter remineralization is due to methanogenesis. The relative contribution of SRR to organic
391   matter remineralization, however, likely is significantly higher when taking into account the high SRR in the
392   uppermost sediment layers (Jørgensen et al., 2001), which are not captured by our model.
393   The depth-dependent rate profile of SO_4^{2-} reduction shows two distinct peaks of ~ 70 and 230 pmol SO_4^{2-} cm^{-3} d^{-1}
394   associated with organoclastic SO_4^{2-} reduction in the organic matter rich marine deposits of Unit I and Unit II. These
395   rates are at the low end of reported values from Black Sea sediments (0.1 - 20 nmol cm^{-3} d^{-1}) (Holmkvist et al.,
396   2011b; Jørgensen et al., 2001, 2004; Knab et al., 2009; Leloup et al., 2007). Our model further demonstrates that the
397   two SRR peaks in the sediments of Unit I and Unit II are not reflected in the pore water profile of SO_4^{2-}. This finding
398   is in line with earlier work showing that the SO_4^{2-} gradient in Black Sea sediments is primarily affected by SO_4-
399   AOM in the SMTZ (Jørgensen et al., 2001). The shorter diffusion distance (the diffusion time to ~ 200 cm is about 5
400   times longer than to ~ 90 cm, i.e. ~ 300 years vs. ~ 60 years) and higher porosity in Unit I and II (Supplementary Fig.
401   S1) both dampen the effect of SO_4^{2-} reduction in the marine deposits on the SO_4^{2-} profile (see also Jørgensen et al.,
402   (2001)). Thus, our results support previous conclusions that SRR estimates based on pore water profiles of SO_4^{2-} (i.e.
403   net SO_4^{2-} consumption) alone may underestimate the actual SO_4^{2-} turnover (i.e. gross SO_4^{2-} reduction) in marine
404   sediments (Jørgensen, 1978; Jørgensen et al., 2001).

405   **4.1.2 SO_4-AOM**

406   Pore water profiles of SO_4^{2-}, CH_4, sulfide and DIC reveal a distinct SMTZ around 230 cm depth at both sites, where
407   SO_4-AOM with upward diffusing CH_4 results in the concomitant removal of pore water SO_4^{2-} and CH_4 and in the
408   accumulation of dissolved sulfide and DIC in the pore waters of these sediments (Fig. 3). The depth of the SMTZ
409   and the steep increase in CH_4 to > 3 mM below the SMTZ found in this study are consistent with earlier observations
410   in sediments of the western Black Sea (Henkel et al., 2012; Holmkvist et al., 2011b; Jørgensen et al., 2001, 2004;
411   Knab et al., 2009; Leloup et al., 2007). The location of the SMTZ, however, has progressed downwards in the last ca.
412   9000 years, following the inflow of SO_4^{2-}-rich salt water into the Black Sea basin (Fig. 7) (see also Henkel et al.,
413   (2012)).
414   Calculated diffusive fluxes of SO_4^{2-} and CH_4 to the SMTZ (~ 0.2 mmol SO_4^{2-} m^{-2} d^{-1} and 0.08 mmol CH_4 m^{-2} d^{-1}) and
415   modelled areal rates of SO_4-AOM (~ 0.16 mmol m^{-2} d^{-1}) suggest that AOM accounts for ~ 40 to 70 % of the total
416   SO_4^{2-} reduction in these sediments, with the remaining ~ 30 to 60 % attributed to organoclastic SO_4^{2-} reduction. Such
417   a high contribution of AOM exceeds the range of previous estimates that included experimentally measured SRR
418   close to the sediment surface (~ 7 to 18 %) (Jørgensen et al., 2001, 2004). Around the SMTZ, SO_4-AOM is
419   responsible for ~ 97 % of the total SO_4^{2-} reduction (Fig. 6 and Table 6), thus enhancing the downward diffusive flux
420   of sulfide into the deep limnic deposits of Unit III. Our model suggests that without this additional source of sulfide
421   through SO_4-AOM, the sulfidization front would currently be located around 150 cm depth in the sediment (Fig. 8).

12

422   The consumption of upward diffusing CH_4 by SO_4^{2-}-driven AOM leads to a progressive enrichment of ^{13}C and D in

423   the residual CH_4 above the SMTZ (Fig. 4) due to the preferential oxidation of isotopically light CH_4 during SO_4-

424   AOM (Alperin et al., 1988; Martens et al., 1999; Whiticar, 1999). Interestingly, pore water CH_4 above the SMTZ

425   shows unusually high δD-CH_4 values that fall outside of the common range observed for pore water δD-CH_4 (e.g.

426   Whiticar et al., 1999). Future studies, however, are needed to resolve the cause of the strong D-enrichment of

427   dissolved CH_4 above the SMTZ in Black Sea sediments.

428   Modeled concentrations of CH_4 indicate that the measurements above the sulfidization front at site 5 are likely less

429   affected by outgassing during core recovery (Fig. 4) and can thus be used to derive kinetic isotope fractionation

430   factors for carbon (ε_C) and hydrogen (ε_H) associated with SO_4-AOM at the SMTZ using the Rayleigh distillation

431   function (Crowe et al., 2011; Egger et al., 2015b; Rayleigh, 1896; Whiticar, 1999). Note that the Rayleigh distillation

432   function only applies to closed systems (Rayleigh, 1896). However, considering that diffusion could be slower than

433   oxidation in deep sediments of the Black Sea, these sediments may represent a quasi-closed system. Corresponding

434   estimates for ε_C of ~ 8 ‰ ($R^2 = 0.972$) and ε_H of ~ 58 ‰ ($R^2 = 0.982$) are at the lower end of previously documented

435   values in marine and brackish-marine environments (8-38 ‰ for ε_C and 100-324 ‰ for ε_H) (Alperin et al., 1988;

436   Egger et al., 2015b; Holler et al., 2009; Martens et al., 1999; Reeburgh, 2007). These values should be interpreted as

437   an approximation, as more accurate estimates would require isotope modeling (e.g. Alperin et al., 1988).

438   At the base of the SMTZ, upward diffusing CH_4 reveals an initial depletion in $\delta^{13}C$-CH_4 (Fig. 4). Such a shift to ^{13}C-

439   depleted CH_4 together with a decrease in its concentration could indicate an enzyme-mediated equilibrium C isotope

440   exchange during SO_4-AOM at low SO_4^{2-} concentrations (< 0.5 mM) (Holler et al., 2012; Yoshinaga et al., 2014). The

441   effect of such mechanisms on deuterated CH_4 is likely limited.

442   **4.1.3 Cryptic S cycling**

443   Earlier studies showed evidence for ongoing SO_4^{2-} reduction (< 1 nmol cm^{-3} d^{-1}) within the SO_4^{2-}-depleted (< 0.5

444   mM) limnic deposits below the SMTZ in sediments of the Black Sea (Holmkvist et al., 2011b; Knab et al., 2009;

445   Leloup et al., 2007), Baltic Sea (Holmkvist et al., 2011a, 2014; Leloup et al., 2009) and Alaskan Beaufort Sea

446   (Treude et al., 2014) likely driven by SO_4^{2-} production from re-oxidation of dissolved sulfide with oxidized Fe

447   minerals. In this mechanism, Fe oxides enhance the recycling of sulfide to SO_4^{2-} in a cryptic S cycle (Holmkvist et

448   al., 2011a; Treude et al., 2014) thereby fueling SO_4^{2-}-driven AOM in Fe oxide-rich sediments. In this cryptic S cycle,

449   dissolved sulfide is oxidized to zero-valent sulfur (S_0), a key intermediate in AOM, which is subsequently

450   disproportionated to SO_4^{2-} and sulfide by associated Deltaproteobacteria (Holmkvist et al., 2011a; Milucka et al.,

451   2012; Sivan et al., 2014; Treude et al., 2014). The additional SO_4^{2-}, produced during S_0 disproportionation, may then

452   be re-used by the methanotrophic archaea as an electron acceptor for SO_4-AOM (Milucka et al., 2012).

453   Our model results suggest slow rates of ongoing SO_4^{2-} reduction of < 0.2 nmol cm^{-3} d^{-1} (Fig. 6) within the limnic

454   deposits below the SMTZ exposed to dissolved sulfide (Table 6), in line with estimated SRR based on $^{35}SO_4^{2-}$

455   incubation experiments with Black Sea sediments from below the SMTZ of ~ 0.1-0.5 nmol cm^{-3} d^{-1} (Knab et al.,

456   2009; Leloup et al., 2007). Below the sulfidization front, SRR show a distinct peak of ~ 5 pmol cm^{-3} d^{-1}. Active SO_4^{2-}

457   reduction in these SO_4^{2-}-depleted sediments requires deep SO_4^{2-} formation to maintain low net rates of SO_4^{2-}

458   reduction. In the model, S_0 disproportionation is the only potential source of pore water SO_4^{2-} at depth (Table 3).

459   Formation of S_0, in turn, occurs exclusively by oxidation of dissolved sulfide during the reductive dissolution of Fe

460   oxides, explaining the distinct S_0 disproportionation peak of $\sim$ 15 pmol cm^{-3} d^{-1} around the sulfidization front (Fig. 6).

461   Thus, based on the model assumptions, we conclude that Fe oxides increase the transformation of sulfide to SO_4^{2-} via

462   formation and subsequent disproportionation of S_0 in these sediments, as suggested previously (Holmkvist et al.,

463   2011b; Knab et al., 2009; Leloup et al., 2007). Such recycling of SO_4^{2-} stimulates slow rates of SO_4-AOM in the

464   sediments below the SMTZ, explaining the low background rates of SO_4^{2-} reduction in the SO_4^{2-}-depleted limnic

465   deposits. These results support recent findings of indirect Fe stimulated SO_4^{2-} driven AOM in laboratory experiments

466   (Sivan et al., 2014), and highlight that Fe oxides could play a significant role as stimulators of AOM and S recycling

467   in natural environments.

4.2 Fe reduction below the sulfidization front

469   Below the sulfidization front, Fe^{2+} starts to accumulate in the pore water (Fig. 3). Although previous studies have

470   also reported an increase of dissolved Fe^{2+} around the depth where sulfide levels drop below the detection limit

471   (Holmkvist et al., 2011b; Jørgensen et al., 2004; Knab et al., 2009), the source of this pore water Fe^{2+} has remained

472   unknown. One possible explanation could be that the elevated Fe^{2+} concentrations at depth represent remnant Fe^{2+}

473   accumulated during the Black Sea "Lake" phase (Knab et al., 2009). In our model, Fe^{2+} shows a broad peak of $\sim$ 300

474   μM until $\sim$ 300 cm depth in the sediment during the initial Lake phase, assuming organoclastic Fe reduction as the

475   only Fe reduction pathway (data not shown). The removal of Fe^{2+} through authigenic formation of reduced Fe(II)

476   minerals, however, prevents the accumulation of substantial amounts of Fe^{2+} in the pore water below $\sim$ 300 cm

477   sediment depth during the Lake phase (Fig. 8). We therefore conclude that the high concentrations of dissolved Fe^{2+}

478   below the sulfidization front are most likely indicative of active Fe reduction in these sediments.

4.2.1 Fe reduction through cryptic S cycling

480   In theory, a cryptic S cycle, as described in section 4.1.3, could result in net accumulation of dissolved Fe^{2+} if the

481   sulfide consumption from reaction with ferric Fe outweighs the production of sulfide from SO_4^{2-} reduction. Modeled

482   Fe^{2+} indeed shows a peak of $<$ 100 μM directly below the sulfidization front, assuming no active Fe reduction in the

483   limnic deposits (Fig. 8). Model simulations further indicate that, based on the reaction network used in this study

484   (Table 3), cryptic S cycling could result in a build up of pore water Fe^{2+} of $\sim$ 300 μM at depth in the sediment

485   provided there was no precipitation of reduced Fe(II) minerals (Supplementary Fig S2). However, concentrations of

486   dissolved Fe^{2+} are too low compared to the measurements and confined to sediments between 300 – 400 cm depths

487   only. The diagenetic model developed in this study therefore suggests that cryptic S cycling is unlikely to explain the

488   high concentrations ($\sim$ 800 μM) of dissolved Fe^{2+} observed in the deep limnic deposits.

4.2.2 Organoclastic Fe reduction

490   In the model, the reduction of Fe oxides coupled to organic matter degradation only occurs with the easily reducible

491   α phase in order to allow for the burial of the more crystalline β phase at depth (Table 3). Since the α phase is

14

492 efficiently reduced in the upper few centimeters during organoclastic Fe reduction, no easily reducible Fe oxides are
493 being buried into the deep sediments in the diagenetic model. Organoclastic Fe reduction therefore does not occur
494 within the modeled deep limnic deposits that exclusively contain more crystalline (β) and refractory (γ) Fe oxides
495 (Fig. 5). Instead, we assume that CH_4 represents a plausible electron donor for the reduction of more crystalline Fe
496 oxides in the organic-poor deep sediments with relatively refractory old organic matter (< 0.8 wt %). The exclusion
497 of organoclastic Fe reduction at depth in the model provides an estimate of an upper constraint on the potential
498 importance of Fe-AOM in Black Sea sediments. As a result of this assumption, however, the model results cannot be
499 used to conclude whether Fe-AOM is more likely than organoclastic Fe reduction.

500 An increasing body of geochemical evidence and laboratory incubation experiments shows that Fe-AOM might be
501 occurring in a variety of different aquatic environments (Amos et al., 2012; Beal et al., 2009; Crowe et al., 2011;
502 Egger et al., 2015b; Riedinger et al., 2014; Scheller et al., 2016; Segarra et al., 2013; Sivan et al., 2011; Wankel et
503 al., 2012). In addition, several studies have shown that Fe-reducing microorganisms are able to outcompete
504 methanogens for common substrates (e.g. acetate and H_2), thus reducing the concentrations of these common
505 primary electron donors to levels that are too low for methanogens to grow (Achtnich et al., 1995; Lovley and
506 Phillips, 1987; Lovley et al., 1989). These results, together with the observed capability of methanogens to switch
507 from CH_4 production to Fe reduction (Bodegom et al., 2004; Bond and Lovley, 2002; Liu et al., 2011; Reiche et al.,
508 2008; Sivan et al., 2016; Vargas et al., 1998) led to the common conclusion that Fe oxides exert a suppressive effect
509 on methanogenesis. Ongoing CH_4 production in the Fe oxide-rich limnic deposits, as deduced from the isotopic
510 composition of pore water CH_4 (Fig. 4) could then indicate limited organoclastic Fe reduction in these sediments.

511 However, there is increasing evidence that (semi)conductive crystalline Fe oxides (e.g. hematite and magnetite) can,
512 in fact, stimulate concurrent methanogenesis and organoclastic Fe reduction through direct interspecies electron
513 transfer (DIET), by serving as electron conduits among syntrophic CH_4-producing organisms at rates that are
514 substantially higher than those for interspecies electron transfer by H_2 (Cruz Viggi et al., 2014; Kato et al., 2012; Li
515 et al., 2014; Zhou et al., 2014; Zhuang et al., 2015). The inhibitory effect of Fe reduction on methanogenesis thus
516 appears to be lower for crystalline Fe oxides such as hematite and magnetite, which are less bioavailable to Fe-
517 reducing organisms than poorly crystalline (amorphous) Fe oxides (e.g. ferrihydrite and lepidocrocite) (Lovley,
518 1991; Qu et al., 2004; Zhuang et al., 2015). These findings indicate that the crystallinity and conductivity of Fe
519 oxides may play a key role in determining whether methanogenesis is stimulated or suppressed in Fe oxide-rich
520 environments. In addition, the presence of methanogens that are able to rapidly switch between methanogenesis and
521 reduction of Fe oxides could also result in a reactivation of less reactive Fe oxides that were not reduced during
522 initial organoclastic Fe reduction in the deep methanogenic zone as suggested by Sivan et al. (2016). Thus, the deep
523 limnic sediments may be characterized by a complex interplay of concurrent methanogenesis, Fe oxide reduction and
524 methanotrophy, i.e. AOM.

525 **4.2.3 Fe-AOM**

526 Our model results indicate that Fe-AOM could also be a possible mechanism explaining the buildup of pore water
527 Fe^{2+} below the sulfidization front. Previous studies have shown that in systems where production and oxidation of

15

528   CH_4 take place concurrently, methanogenesis might conceal the isotopic signature of AOM (Egger et al., 2015b;

529   Seifert et al., 2006; Whiticar, 1999). Thus, unlike SO_4-AOM, Fe-dependent AOM likely only has little effect on the

530   isotopic composition of pore water CH_4 due to the removal of small amounts of CH_4 in sediments with ongoing

531   methanogenesis. This might explain why pore water CH_4 does not show enrichment in both heavy isotopes below the

532   sulfidization front as would be expected if Fe-AOM would occur, but rather indicates antipathetic changes, i.e.

533   depletion in ^{13}C-CH_4 and enrichment in D-CH_4, usually attributed to CH_4 production from carbonate reduction

534   (Chanton et al., 2005; Whiticar, 1999).

535   Model derived rates for Fe-AOM of ~ 0.04 pmol cm^{-3} d^{-1} (Fig. 6) are significantly lower than potential Fe-AOM

536   rates of ~ 4 nmol cm^{-3} d^{-1} estimated from laboratory incubation studies (Egger et al., 2015b; Segarra et al., 2013;

537   Sivan et al., 2011) with brackish and limnic sediment samples. This large deviation is likely due to an overestimation

538   of Fe-AOM rates derived from stimulated microbial communities under laboratory conditions using freshly

539   synthesized and thus easily bioavailable Fe oxides when compared to in-situ conditions.

540   In the upper 800 cm of sediment, Fe-AOM accounts for < 1 % of total CH_4 oxidation, with the remaining > 99 %

541   attributed to SO_4-AOM (Table 6; see also Supplementary Fig. S2). However, while high rates of SO_4-AOM are

542   mainly restricted to the SMTZ, Fe-AOM might occur over a deep methanogenic zone, reaching far down into the

543   sediment. To accurately assess the contribution of Fe-AOM to the total CH_4 consumption in Black Sea sediments,

544   additional knowledge about the vertical expansion of the Fe oxide-rich limnic sediments deposited during the Blake

545   Sea "Lake" phase would be required.

546   **4.3 Impact of S-Fe-CH_4 dynamics on sedimentary P diagenesis**

547   Degradation of organic matter and the subsequent release of HPO_4^{2-} to the pore water during early diagenesis

548   typically results in a sink-switching from organic P to authigenic P-bearing phases such as Ca phosphates (Filippelli,

549   1997; Ruttenberg and Berner, 1993; Slomp et al., 1996b), Mn-Ca carbonates (Jilbert and Slomp, 2013; Mort et al.,

550   2010; Suess, 1979) or reduced Fe phosphates (Burns, 1997; Jilbert and Slomp, 2013; Martens et al., 1978; März et

551   al., 2008). Reductive dissolution of Fe oxides by dissolved sulfide and the following liberation of HPO_4^{2-} may also

552   contribute to the buildup of pore water HPO_4^{2-} (Burns, 1997; Egger et al., 2015a; März et al., 2008; Schulz et al.,

553   1994). Thus, the downward sulfidization ultimately results in the accumulation of dissolved HPO_4^{2-} in the pore water

554   as the sulfidization front moves downward into the limnic deposits (Fig. 7).

555   The pore water profile of HPO_4^{2-} (Fig. 3) indicates the presence of a sink for HPO_4^{2-} below the sulfidization front

556   and, to a lesser extent, in the sulfidic sediments around the SMTZ, likely unrelated to Ca-P authigenesis (Fig. 5).

557   Such a sink for HPO_4^{2-} below sulfidic sediments has been observed previously (Burns, 1997; Egger et al., 2015a;

558   März et al., 2008; Schulz et al., 1994; Slomp et al., 2013) and shown to be most likely the result of vivianite

559   formation (Egger et al., 2015a; Hsu et al., 2014; März et al., 2008). Abundant dissolved Fe^{2+} and a peak in Fe-

560   associated P below the sulfidization front observed in this study (Fig. 3 and Fig. 5) suggest that vivianite authigenesis

561   might also be occurring in the limnic deposits below the sulfidzation front in Black Sea sediments.

562   Assuming that vivianite formation represents the only sink for pore water HPO_4^{2-} results in a good fit between the

563   modeled and measured pore water profile of HPO_4^{2-} below the sulfidization front (Fig. 3). Modeled vivianite

16

564 formation accounts for up to 70 % of total Fe-associated P directly below the sulfidization front. However, the model

565 underestimates the sharp peak in Fe-associated P directly below the sulfidization front, suggesting that modeled

566 vivianite formation likely underestimates the actual contribution of vivianite in these sediments. In the limnic

567 deposits not yet impacted by the downward sulfidization, modeled vivianite accounts for ∼ 20 – 30 % of total Fe-

568 associated P. From this, we estimate that vivianite may be responsible for > 20 % of total P burial directly below the

569 sulfidization front and for ∼ 10 % of total P burial in the deep limnic deposits at depth.

570 Running the model without Fe-AOM and thus without Fe reduction at depth results in modeled pore water HPO_4^{2-}

571 concentrations of up to ∼ 350 μM at depth in the sediment (Fig. 8). This suggests that Fe-AOM can promote

572 conditions that allow sequestration of a significant proportion of P as vivianite in the limnic deposits below the

573 sulfidization front. Consistent with earlier findings, Fe-AOM likely only accounts for a small fraction of total CH_4

574 oxidation, but may substantially impact the biogeochemical cycling of sedimentary P (Egger et al., 2015a, 2015b;

575 Rooze et al., 2016).

576 The deviation between the modeled and measured profiles of HPO_4^{2-} and Fe-associated P in the upper 300 cm of

577 sediment (Fig. 3 and Fig. 5) could indicate apatite authigenesis (Dijkstra et al., 2014) or the formation of vivianite in

578 microenvironments as previously suggested for sulfidic sediments (Dijkstra et al., 2014; Jilbert and Slomp, 2013).

579 For example, *Deltaproteobacteria*, known to be involved in SO_4-AOM, have been shown to accumulate Fe- and P-

580 rich inclusions in their cells (Milucka et al., 2012). They may therefore provide a potential explanation for the

581 occurrence of Fe-associated P in sulfidic sediments (Dijkstra et al., 2014; Jilbert and Slomp, 2013). However, such

582 microenvironments are not captured in our model.

583 In the diagenetic model, vivianite undergoes dissolution if sulfide is present in the pore waters (Table 3). Sulfide-

584 induced vivianite dissolution significantly improved the model fit to the measured HPO_4^{2} and sulfide data. With the

585 downward migration of dissolved sulfide, modeled vivianite becomes increasingly enriched below the sulfidization

586 front (Fig. 7). Thus, similar to the sulfidization front, a downward diffusive vivianite front may exist in sedimentary

587 systems experiencing downward sulfidzation.

588 In summary, the enhanced downward sulfidization driven by SO_4-AOM leads to dissolution of Fe oxide-bound P in

589 the lake deposits. Below the sulfidization front, downward diffusing HPO_4^{2-} is bound again in authigenic vivianite

590 due to high concentrations of dissolved Fe^{2+} at depth in the sediment generated by ongoing Fe oxide reduction. As a

591 result, trends in total P with depth are significantly altered, showing an accumulation in total P below the

592 sulfidization front unrelated to changes in organic matter deposition and enhanced sedimentary P burial during

593 deposition.

594 **5.   Conclusions**

595 In the Black Sea, the shift from a freshwater lake to a marine system and subsequent downward diffusion of marine

596 SO_4^{2-} into the CH_4-bearing lake sediments results in a multitude of diagenetic reactions around the SMTZ (Fig. 9).

597 The diagenetic model developed in this study shows that SO_4-AOM within the SMTZ significantly enhances the

598 downward diffusive flux of sulfide into the deep limnic deposits, forming a distinct diagenetic sulfidization front

599 around 300 cm depth in the sediment. Our results indicate that without this additional source of dissolved sulfide in

17

the SMTZ, the current sulfidization front would be located around a depth of 150 cm. During the downward sulfidization, Fe oxides, Fe carbonates and vivianite are converted to Fe sulfide phases, leading to an enrichment in solid phase S contents and the release of HPO_4^{2-} to the pore water. Our results further support the hypothesis that part of the downward migrating sulfide is re-oxidized to SO_4^{2-} upon reaction with ferric Fe minerals, fueling a cryptic S cycle and thus stimulating slow rates ($\sim$ 1-5 pmol cm^{-3} d^{-1}) of SO_4-AOM in the SO_4^{2-}-depleted limnic deposits below the SMTZ (Holmkvist et al., 2011a, 2011b; Knab et al., 2009; Leloup et al., 2007).

We propose that besides organoclastic Fe oxide reduction and reactivation of less reactive Fe oxides by methanogens, AOM coupled to the reduction of Fe oxides may also be a possible mechanism explaining the high concentrations of Fe^{2+} in the pore water below the sulfidization front. The buildup of dissolved Fe^{2+} at depth creates conditions that allow sequestration of the downward diffusing HPO_4^{2-} as authigenic vivianite, resulting in an accumulation of total P in these sediments.

The diagenetic processes described here reveal that AOM may strongly overprint burial records of Fe, S and P in depositional marine systems subject to changes in organic matter loading or water column salinity such as coastal environments (Egger et al., 2015a; Rooze et al., 2016), deep-sea fan sediments (März et al., 2008; Schulz et al., 1994) and many high-latitude seas (Holmkvist et al., 2014; Treude et al., 2014). Interpreting these diagenetic patterns as primary sedimentary signals may lead to incorrect reconstructions of environmental conditions during sediment deposition.

References

Achtnich, C., Bak, F. and Conrad, R.: Competition for electron donors among nitrate reducers, ferric iron reducers, sulfate reducers, and methanogens in anoxic paddy soil, Biol. Fertil. Soils, 19, 65–72, doi:10.1007/BF00336349, 1995.

Alperin, M. J., Reeburgh, W. S. and Whiticar, M. J.: Carbon and hydrogen isotope fractionation resulting from

18

anaerobic methane oxidation, Glob. Biogeochem. Cycl., 2(3), 279–288, doi:10.1029/GB002i003p00279, 1988.

Amos, R. T., Bekins, B. A., Cozzarelli, I. M., Voytek, M. A., Kirshtein, J. D., Jones, E. J. P. and Blowes, D. W.: Evidence for iron-mediated anaerobic methane oxidation in a crude oil-contaminated aquifer, Geobiology, 10(6), 506–17, doi:10.1111/j.1472-4669.2012.00341.x, 2012.

Arthur, M. A. and Dean, W. E.: Organic-matter production and evolution of anoxia in the Holocene Black Sea, Paleoceanography, 13(4), 395–411, doi:10.1029/98PA01161, 1998.

Beal, E. J., House, C. H. and Orphan, V. J.: Manganese- and iron-dependent marine methane oxidation, Science (80-.)., 325, 184–187, doi:10.1126/science.1169984, 2009.

Berg, P., Rysgaard, S. and Thamdrup, B.: Dynamic modeling of early diagenesis and nutrient cycling. A case study in an Arctic marine sediment, Am. J. Sci., 303(10), 905–955, doi:10.2475/ajs.303.10.905, 2003.

Berner, R. A.: Iron sulfides in Pleistocene deep Black Sea sediments and their paleo-oceanographic significance, in The Black Sea - Geology, Chemistry and Biology, edited by E. T. Degens and D. A. Ross, pp. 524–531, Plenum Press., 1974.

Berner, R. A.: Early Diagenesis: A Theoretical Approach, Princeton University Press., 1980.

Bodegom, P. M., Scholten, J. C. M. and Stams, A. J. M.: Direct inhibition of methanogenesis by ferric iron, FEMS Microbiol. Ecol., 49(2), 261–268, doi:10.1016/j.femsec.2004.03.017, 2004.

Bond, D. R. and Lovley, D. R.: Reduction of Fe(III) oxide by methanogens in the presence and absence of extracellular quinones, Environ. Microbiol., 4(2), 115–24, doi:10.1046/j.1462-2920.2002.00279.x, 2002.

Boudreau, B. P.: The diffusive tortuosity of fine-grained unlithified sediments, Geochim. Cosmochim. Acta, 60(16), 3139–3142, doi:10.1016/0016-7037(96)00158-5, 1996.

Boudreau, B. P.: Diagenetic models and their implementation. Modelling transport and reactions in aquatic sediments, Springer., 1997.

Brass, M. and Röckmann, T.: Continuous-flow isotope ratio mass spectrometry method for carbon and hydrogen isotope measurements on atmospheric methane, Atmos. Meas. Tech., 3(6), 1707–1721, doi:10.5194/amt-3-1707-2010, 2010.

Burns, S. J.: Early diagenesis in Amazon fan sediments, in Proceeding of the Ocean Drilling Program, Scientific Results, vol. 155, edited by R. D. Flood, D. J. W. Piper, A. Klaus, and L. C. Peterson, pp. 497–504., 1997.

Burton, E. D., Sullivan, L. A., Bush, R. T., Johnston, S. G. and Keene, A. F.: A simple and inexpensive chromium-reducible sulfur method for acid-sulfate soils, Appl. Geochemistry, 23(9), 2759–2766, doi:10.1016/j.apgeochem.2008.07.007, 2008.

Capet, A., Beckers, J.-M. and Grégoire, M.: Drivers, mechanisms and long-term variability of seasonal hypoxia on the Black Sea northwestern shelf – is there any recovery after eutrophication?, Biogeosciences, 10, 3943–3962, doi:10.5194/bg-10-3943-2013, 2013.

Chanton, J., Chaser, L., Glasser, P. and Siegel, D.: Carbon and hydrogen isotopic effects in microbial methane from

19

terrestrial environments, in Stable isotopes and biosphere-atmosphere interactions, edited by L. Flanagan, pp. 85–105, Elsevier-Academic Press., Amsterdam., 2005.

Chanton, J. P.: The effect of gas transport on the isotope signature of methane in wetlands, Org. Geochem., 36, 753–768, doi:10.1016/j.orggeochem.2004.10.007, 2005.

Claff, S. R., Sullivan, L. A., Burton, E. D. and Bush, R. T.: A sequential extraction procedure for acid sulfate soils: Partitioning of iron, Geoderma, 155(3-4), 224–230, doi:10.1016/j.geoderma.2009.12.002, 2010.

Crowe, S. A., Katsev, S., Leslie, K., Sturm, A., Magen, C., Nomosatryo, S., Pack, M. A., Kessler, J. D., Reeburgh, W. S., Roberts, J. A., González, L., Douglas Haffner, G., Mucci, A., Sundby, B. and Fowle, D. A.: The methane cycle in ferruginous Lake Matano, Geobiology, 9(1), 61–78, doi:10.1111/j.1472-4669.2010.00257.x, 2011.

Cruz Viggi, C., Rossetti, S., Fazi, S., Paiano, P., Majone, M. and Aulenta, F.: Magnetite particles triggering a faster and more robust syntrophic pathway of methanogenic propionate degradation, Environ. Sci. Technol., 48(13), 7536–7543, doi:10.1021/es5016789, 2014.

Degens, E. T. and Ross, D. A.: The Black Sea - geology, chemistry, and biology: American Association of Petroleum Geologists Memoir 20., 1974.

Dijkstra, N., Kraal, P., Kuypers, M. M. M., Schnetger, B. and Slomp, C. P.: Are iron-phosphate minerals a sink for phosphorus in anoxic Black Sea sediments?, PLoS One, 9(7), doi:10.1371/journal.pone.0101139, 2014.

Eckert, S., Brumsack, H.-J., Severmann, S., Schnetger, B., März, C. and Frollje, H.: Establishment of euxinic conditions in the Holocene Black Sea, Geology, 41(4), 431–434, 2013.

Egger, M., Jilbert, T., Behrends, T., Rivard, C. and Slomp, C. P.: Vivianite is a major sink for phosphorus in methanogenic coastal surface sediments, Geochim. Cosmochim. Acta, 169, 217–235, doi:10.1016/j.gca.2015.09.012, 2015a.

Egger, M., Rasigraf, O., Sapart, C. J., Jilbert, T., Jetten, M. S. M., Röckmann, T., van der Veen, C., Bândă, N., Kartal, B., Ettwig, K. F. and Slomp, C. P.: Iron-mediated anaerobic oxidation of methane in brackish coastal sediments, Environ. Sci. Technol., 49(1), 277–283, doi:10.1021/es503663z, 2015b.

Ettwig, K. F., Butler, M. K., Le Paslier, D., Pelletier, E., Mangenot, S., Kuypers, M. M. M., Schreiber, F., Dutilh, B. E., Zedelius, J., de Beer, D., Gloerich, J., Wessels, H. J. C. T., van Alen, T., Luesken, F., Wu, M. L., van de Pas-Schoonen, K. T., Op den Camp, H. J. M., Janssen-Megens, E. M., Francoijs, K.-J., Stunnenberg, H., Weissenbach, J., Jetten, M. S. M. and Strous, M.: Nitrite-driven anaerobic methane oxidation by oxygenic bacteria, Nature, 464, 543–548, doi:10.1038/nature08883, 2010.

Filippelli, G. M.: Controls on phosphorus concentration and accumulation in oceanic sediments, Mar. Geol., 139(1–4), 231–240, 1997.

Froelich, P. N., Klinkhammer, G. P., Bender, M. L., Luedtke, N. A., Heath, G. R., Cullen, D., Dauphin, P., Hammond, D., Hartman, B. and Maynard, V.: Early oxidation of organic matter in pelagic sediments of the eastern equatorial Atlantic: suboxic diagenesis, Geochim. Cosmochim. Acta, 43(7), 1075–1090, doi:10.1016/0016-7037(79)90095-4, 1979.

20

703   Grasshoff, K.: A simultaneous multiple channel system for nutrient analysis in seawater with analog and digital data
704   record, Contrib. 2338, Woods Hole, 1969.

705   Happell, J. D., Chanton, J. P. and Showers, W. J.: Methane transfer across the water-air interface in stagnant wooded
706   swamps of Florida : Evaluation of mass-transfer coefficients and isotopic fractionation, , 40(2), 290–298, 1995.

707   Henkel, S., Mogollón, J. M., Nöthen, K., Franke, C., Bogus, K., Robin, E., Bahr, A., Blumenberg, M., Pape, T.,
708   Seifert, R., März, C., de Lange, G. J. and Kasten, S.: Diagenetic barium cycling in Black Sea sediments - A case
709   study for anoxic marine environments, Geochim. Cosmochim. Acta, 88, 88–105, doi:10.1016/j.gca.2012.04.021,
710   2012.

711   Hindmarsh, A. C.: ODEPACK, a systematized collection of ODE solvers, in IMACS Transactions on Scientific
712   Computation, Vol. 1, edited by R. S. Stepleman and Others, pp. 55–64, North-Holland, Amsterdam., 1983.

713   Holler, T., Wegener, G., Knittel, K., Boetius, A., Brunner, B., Kuypers, M. M. M. and Widdel, F.: Substantial (13)
714   C/(12) C and D/H fractionation during anaerobic oxidation of methane by marine consortia enriched in vitro,
715   Environ. Microbiol. Rep., 1(5), 370–6, doi:10.1111/j.1758-2229.2009.00074.x, 2009.

716   Holler, T., Wegener, G., Niemann, H., Ferdelman, T. G., Boetius, A., Kristiansen, T. Z., Molina, H., Pandey, A.,
717   Werner, J. K., Juluri, K. R., Xu, Y., Glenn, D., Parang, K. and Snyder, S. H.: Carbon and sulfur back flux during
718   anaerobic microbial oxidation of methane and coupled sulfate reduction, Proc. Natl. Acad. Sci., 109(51), 21170–
719   21170, doi:10.1073/pnas.1218683109, 2012.

720   Holmkvist, L., Ferdelman, T. G. and Jørgensen, B. B.: A cryptic sulfur cycle driven by iron in the methane zone of
721   marine sediment (Aarhus Bay, Denmark), Geochim. Cosmochim. Acta, 75(12), 3581–3599,
722   doi:10.1016/j.gca.2011.03.033, 2011a.

723   Holmkvist, L., Kamyshny, A., Brüchert, V., Ferdelman, T. G. and Jørgensen, B. B.: Sulfidization of lacustrine
724   glacial clay upon Holocene marine transgression (Arkona Basin, Baltic Sea), Geochim. Cosmochim. Acta, 142, 75–
725   94, doi:10.1016/j.gca.2014.07.030, 2014.

726   Holmkvist, L., Kamyshny, A., Vogt, C., Vamvakopoulos, K., Ferdelman, T. G. and Jørgensen, B. B.: Sulfate
727   reduction below the sulfate–methane transition in Black Sea sediments, Deep Sea Res. Part I Oceanogr. Res. Pap.,
728   58(5), 493–504, doi:10.1016/j.dsr.2011.02.009, 2011b.

729   Hsu, T.-W., Jiang, W.-T. and Wang, Y.: Authigenesis of vivianite as influenced by methane-induced sulfidization in
730   cold-seep sediments off southwestern Taiwan, J. Asian Earth Sci., 89, 88–97, doi:10.1016/j.jseaes.2014.03.027,
731   2014.

732   Ingall, E. D., Bustin, R. M. and Van Cappellen, P.: Influence of water column anoxia on the burial and preservation
733   of carbon and phosphorus in marine shales, Geochim. Cosmochim. Acta, 57(2), 303–316, 1993.

734   Jilbert, T. and Slomp, C. P.: Iron and manganese shuttles control the formation of authigenic phosphorus minerals in
735   the euxinic basins of the Baltic Sea, Geochim. Cosmochim. Acta, 107, 155–169, doi:10.1016/j.gca.2013.01.005,
736   2013.

737   Jørgensen, B. B.: A comparison of methods for the quantification of bacterial sulfate reduction in coastal marine

21

738   sediments. II. Calculations from mathematical models, Geomicrobiol. J., 1, 29–51, doi:10.1080/01490457809377721, 1978.

740   Jørgensen, B. B., Böttcher, M. E., Lüschen, H., Neretin, L. N. and Volkov, I. I.: Anaerobic methane oxidation and a
741   deep H2S sink generate isotopically heavy sulfides in Black Sea sediments, Geochim. Cosmochim. Acta, 68(9),
742   2095–2118, doi:10.1016/j.gca.2003.07.017, 2004.

743   Jørgensen, B. B., Weber, A. and Zopfi, J.: Sulfate reduction and anaerobic methane oxidation in Black Sea
744   sediments, Deep Sea Res. Part I Oceanogr. Res. Pap., 48, 2097–2120, doi:10.1016/S0967-0637(01)00007-3, 2001.

745   Kato, S., Hashimoto, K. and Watanabe, K.: Methanogenesis facilitated by electric syntrophy via (semi)conductive
746   iron-oxide minerals, Environ. Microbiol., 14(7), 1646–1654, doi:10.1111/j.1462-2920.2011.02611.x, 2012.

747   Kemp, W. M., Testa, J. M., Conley, D. J., Gilbert, D. and Hagy, J. D.: Temporal responses of coastal hypoxia to
748   nutrient loading and physical controls, Biogeosciences, 6(12), 2985–3008, doi:10.5194/bg-6-2985-2009, 2009.

749   Knab, N. J., Cragg, B. A., Hornibrook, E. R. C., Holmkvist, L., Pancost, R. D., Borowski, C., Parkes, R. J. and
750   Jørgensen, B. B.: Regulation of anaerobic methane oxidation in sediments of the Black Sea, Biogeosciences, (6),
751   1505–1518, doi:10.5194/bg-6-1505-2009, 2009.

752   Knittel, K. and Boetius, A.: Anaerobic oxidation of methane: progress with an unknown process, Annu. Rev.
753   Microbiol., 63, 311–334, doi:10.1146/annurev.micro.61.080706.093130, 2009.

754   Kraal, P. and Slomp, C. P.: Rapid and extensive alteration of phosphorus speciation during oxic storage of wet
755   sediment samples, PLoS One, 9(5), e96859, 2014.

756   Kraal, P., Slomp, C. P., Forster, A. and Kuypers, M. M. M.: Pyrite oxidation during sample storage determines
757   phosphorus fractionation in carbonate-poor anoxic sediments, Geochim. Cosmochim. Acta, 73(11), 3277–3290,
758   doi:10.1016/j.gca.2009.02.026, 2009.

759   Leloup, J., Fossing, H., Kohls, K., Holmkvist, L., Borowski, C. and Jørgensen, B. B.: Sulfate-reducing bacteria in
760   marine sediment (Aarhus Bay, Denmark): abundance and diversity related to geochemical zonation, Environ.
761   Microbiol., 11(5), 1278–1291, doi:10.1111/j.1462-2920.2008.01855.x, 2009.

762   Leloup, J., Loy, A., Knab, N. J., Borowski, C., Wagner, M. and Jørgensen, B. B.: Diversity and abundance of sulfate-
763   reducing microorganisms in the sulfate and methane zones of a marine sediment, Black Sea, Environ. Microbiol.,
764   9(1), 131–142, doi:10.1111/j.1462-2920.2006.01122.x, 2007.

765   Li, H., Chang, J., Liu, P., Fu, L., Ding, D. and Lu, Y.: Direct interspecies electron transfer accelerates syntrophic
766   oxidation of butyrate in paddy soil enrichments, Environ. Microbiol., 17, 1–45, doi:10.1111/1462-2920.12576, 2014.

767   Liu, D., Wang, H., Dong, H., Qiu, X., Dong, X. and Cravotta, C. A.: Mineral transformations associated with
768   goethite reduction by Methanosarcina barkeri, Chem. Geol., 288(1-2), 53–60, doi:10.1016/j.chemgeo.2011.06.013,
769   2011.

770   Lovley, D. R.: Dissimilatory Fe(III) and Mn(IV) reduction, Microbiol. Rev., 55(2), 259–287, 1991.

771   Lovley, D. R. and Phillips, E. J. P.: Competitive mechanisms for inhibition of sulfate reduction and methane

22

772   production in the zone of ferric iron reduction in sediments, Appl. Environ. Microbiol., 53(11), 1987.

773   Lovley, D. R., Phillips, E. J. P. and Lonergan, D. J.: Hydrogen and formate oxidation coupled to dissimilatory
774   reduction of iron or manganese by Alteromonas putrefaciens, Appl. Environ. Microbiol., 55(3), 700–706, 1989.

775   Martens, C. S., Albert, D. B. and Alperin, M. J.: Stable isotope tracing of anaerobic methane oxidation in the gassy
776   sediments of Eckernforde Bay, German Baltic Sea, Am. J. Sci., 299, 589–610, doi:10.2475/ajs.299.7-9.589, 1999.

777   Martens, C. S., Berner, R. A. and Rosenfeld, J. K.: Interstitial water chemistry of anoxic Long Island Sound
778   sediments. 2. Nutrient regeneration and phosphate removal, Limnol. Oceanogr., 23(4), 605–617, 1978.

779   März, C., Hoffmann, J., Bleil, U., de Lange, G. J. and Kasten, S.: Diagenetic changes of magnetic and geochemical
780   signals by anaerobic methane oxidation in sediments of the Zambezi deep-sea fan (SW Indian Ocean), Mar. Geol.,
781   255(3-4), 118–130, doi:10.1016/j.margeo.2008.05.013, 2008.

782   Meysman, F. J. R., Boudreau, B. P. and Middelburg, J. J.: Modeling reactive transport in sediments subject to
783   bioturbation and compaction, Geochim. Cosmochim. Acta, 69(14), 3601–3617, doi:10.1016/j.gca.2005.01.004,
784   2005.

785   Milucka, J., Ferdelman, T. G., Polerecky, L., Franzke, D., Wegener, G., Schmid, M., Lieberwirth, I., Wagner, M.,
786   Widdel, F. and Kuypers, M. M. M.: Zero-valent sulphur is a key intermediate in marine methane oxidation, Nature,
787   491(7425), 541–6, doi:10.1038/nature11656, 2012.

788   Mogollón, J. M., Dale, A. W., Jensen, J. B., Schlüter, M. and Regnier, P.: A method for the calculation of anaerobic
789   oxidation of methane rates across regional scales: An example from the Belt Seas and The Sound (North Sea-Baltic
790   Sea transition), Geo-Marine Lett., 33(4), 299–310, doi:10.1007/s00367-013-0329-z, 2013.

791   Moodley, L., Middelburg, J. J., Herman, P. M. J., Soetaert, K. and de Lange, G. J.: Oxygenation and organic-matter
792   preservation in marine sediments: Direct experimental evidence from ancient organic carbon–rich deposits, Geology,
793   33(11), 889, doi:10.1130/G21731.1, 2005.

794   Mort, H. P., Slomp, C. P., Gustafsson, B. G. and Andersen, T. J.: Phosphorus recycling and burial in Baltic Sea
795   sediments with contrasting redox conditions, Geochim. Cosmochim. Acta, 74(4), 1350–1362,
796   doi:10.1016/j.gca.2009.11.016, 2010.

797   Murphy, J. and Riley, J. P.: A modified single solution method for the determination of phosphate in natural waters,
798   Anal. Chim. Acta, 27, 31–36, doi:10.1016/S0003-2670(00)88444-5, 1962.

799   Neretin, L. N., Böttcher, M. E., Jørgensen, B. B., Volkov, I. I., Lüschen, H. and Hilgenfeldt, K.: Pyritization
800   processes and greigite formation in the advancing sulfidization front in the Upper Pleistocene sediments of the Black
801   Sea, Geochim. Cosmochim. Acta, 68(9), 2081–2093, doi:10.1016/S0016-7037(00)00450-2, 2004.

802   Petzoldt, L. R.: Automatic selection of methods for solving stiff and nonstiff systems of ordinary differential
803   equations, SIAM J. Sci. Stat. Comput., 4, 136–148, doi:10.1137/0904010, 1983.

804   Poulton, S. and Canfield, D.: Development of a sequential extraction procedure for iron: implications for iron
805   partitioning in continentally derived particulates, Chem. Geol., 214(3-4), 209–221,
806   doi:10.1016/j.chemgeo.2004.09.003, 2005.

807   Qu, D., Ratering, S. and Schnell, S.: Microbial reduction of weakly crystalline iron (III) oxides and suppression of
808   methanogenesis in paddy soil, Bull. Environ. Contam. Toxicol., 72(6), 1172–1181, doi:10.1007/s00128-004-0367-3,
809   2004.

810   Raghoebarsing, A. A., Pol, A., van de Pas-Schoonen, K. T., Smolders, A. J. P., Ettwig, K. F., Rijpstra, W. I. C.,
811   Schouten, S., Damsté, J. S. S., Op den Camp, H. J. M., Jetten, M. S. M. and Strous, M.: A microbial consortium
812   couples anaerobic methane oxidation to denitrification, Nature, 440(7086), 918–921, doi:10.1038/nature04617, 2006.

813   Raiswell, R. and Canfield, D. E.: The iron biogeochemical cycle past and present, Geochemical Perspect., 1(1),
814   doi:10.7185/geochempersp.1.1, 2012.

815   Rayleigh, J. W. S.: Theoretical considerations respecting the separation of gases by diffusion and similar processes,
816   Philos. Mag., (42), 493–499, 1896.

817   Reeburgh, W.: Oceanic methane biogeochemistry, Am. Chem. Soc., 107(2), 486–513, doi:10.1021/cr050362v, 2007.

818   Reed, D. C., Slomp, C. P. and Gustafsson, B. G.: Sedimentary phosphorus dynamics and the evolution of bottom-
819   water hypoxia: A coupled benthic-pelagic model of a coastal system, Limnol. Oceanogr., 56(3), 1075–1092,
820   doi:10.4319/lo.2011.56.3.1075, 2011a.

821   Reed, D. C., Slomp, C. P. and de Lange, G. J.: A quantitative reconstruction of organic matter and nutrient
822   diagenesis in Mediterranean Sea sediments over the Holocene, Geochim. Cosmochim. Acta, 75(19), 5540–5558,
823   doi:10.1016/j.gca.2011.07.002, 2011b.

824   Regnier, P., Dale, A. W., Arndt, S., LaRowe, D. E., Mogollón, J. and Van Cappellen, P.: Quantitative analysis of
825   anaerobic oxidation of methane (AOM) in marine sediments: A modeling perspective, Earth-Science Rev., 106(1-2),
826   105–130, doi:10.1016/j.earscirev.2011.01.002, 2011.

827   Reiche, M., Torburg, G. and Küsel, K.: Competition of Fe(III) reduction and methanogenesis in an acidic fen, FEMS
828   Microbiol. Ecol., 65(1), 88–101, doi:10.1111/j.1574-6941.2008.00523.x, 2008.

829   Rickard, D. and Luther, G. W.: Kinetics of pyrite formation by the H2S oxidation of iron (II) monosulfide in aqueous
830   solutions between 25 and 125°C: The mechanism, Geochim. Cosmochim. Acta, 61(1), 135–147, doi:10.1016/S0016-
831   7037(96)00322-5, 1997.

832   Riedinger, N., Formolo, M. J., Lyons, T. W., Henkel, S., Beck, A. and Kasten, S.: An inorganic geochemical
833   argument for coupled anaerobic oxidation of methane and iron reduction in marine sediments, Geobiology,
834   doi:10.1111/gbi.12077, 2014.

835   Rooze, J., Egger, M., Tsandev, I. and Slomp, C. P.: Iron-dependent anaerobic oxidation of methane in coastal surface
836   sediments: potential controls and impact, Limnol. Oceanogr., doi:10.1002/lno.10275, 2016.

837   Ruttenberg, K. C.: Development of a sequential extraction method for different forms of phosphorus in marine
838   sediments, Limnol. Oceanogr., 37(7), 1460–1482, 1992.

839   Ruttenberg, K. C. and Berner, R. A.: Authigenic apatite formation and burial in sediments from non-upwelling,
840   continental margin environments, Geochim. Cosmochim. Acta, 57(5), 991–1007, doi:10.1016/0016-7037(93)90035-
841   U, 1993.

24

842 Van Santvoort, P. J. M., De Lange, G. J., Thomson, J., Colley, S., Meysman, F. J. R. and Slomp, C. P.: Oxidation

843 and origin of organic matter in surficial Eastern Mediterranean hemipelagic sediments, Aquat. Geochemistry, 8(3),

844 153–175, doi:10.1023/A:1024271706896, 2002.

845 Sapart, C. J., van der Veen, C., Vigano, I., Brass, M., van de Wal, R. S. W., Bock, M., Fischer, H., Sowers, T.,

846 Buizert, C., Sperlich, P., Blunier, T., Behrens, M., Schmitt, J., Seth, B. and Röckmann, T.: Simultaneous stable

847 isotope analysis of methane and nitrous oxide on ice core samples, Atmos. Meas. Tech., 4(12), 2607–2618,

848 doi:10.5194/amt-4-2607-2011, 2011.

849 Scheller, S., Yu, H., Chadwick, G. L., McGlynn, S. E. and Orphan, V. J.: Artificial electron acceptors decouple

850 archaeal methane oxidation from sulfate reduction, Science (80-.)., 351(6274), 703–707,

851 doi:10.1126/science.aad7154, 2016.

852 Schulz, H. D., Dahmke, A., Schinzel, U., Wallmann, K. and Zabel, M.: Early diagenetic processes, fluxes, and

853 reaction rates in sediments of the South Atlantic, Geochim. Cosmochim. Acta, 58(9), 2041–2060, doi:10.1016/0016-

854 7037(94)90284-4, 1994.

855 Segarra, K. E. A., Comerford, C., Slaughter, J. and Joye, S. B.: Impact of electron acceptor availability on the

856 anaerobic oxidation of methane in coastal freshwater and brackish wetland sediments, Geochim. Cosmochim. Acta,

857 115, 15–30, doi:10.1016/j.gca.2013.03.029, 2013.

858 Seifert, R., Nauhaus, K., Blumenberg, M., Krüger, M. and Michaelis, W.: Methane dynamics in a microbial

859 community of the Black Sea traced by stable carbon isotopes in vitro, Org. Geochem., 37(10), 1411–1419,

860 doi:10.1016/j.orggeochem.2006.03.007, 2006.

861 Sivan, O., Adler, M., Pearson, A., Gelman, F., Bar-Or, I., John, S. G. and Eckert, W.: Geochemical evidence for

862 iron-mediated anaerobic oxidation of methane, Limnol. Oceanogr., 56(4), 1536–1544,

863 doi:10.4319/lo.2011.56.4.1536, 2011.

864 Sivan, O., Antler, G., Turchyn, A. V., Marlow, J. J. and Orphan, V. J.: Iron oxides stimulate sulfate-driven anaerobic

865 methane oxidation in seeps, Proc. Natl. Acad. Sci., 1–9, doi:10.1073/pnas.1412269111, 2014.

866 Sivan, O., Shusta, S. and Valentine, D. L.: Methanogens rapidly transition from methane production to iron

867 reduction, Geobiology, doi:10.1111/gbi.12172, 2016.

868 Slomp, Van der Gaast, S. J. and Van Raaphorst, W.: Phosphorus binding by poorly crystalline iron oxides in North

869 Sea sediments, Mar. Chem., 52(1), 55–73, doi:10.1016/0304-4203(95)00078-X, 1996a.

870 Slomp, C. P., Epping, E. H. G., Helder, W. and Raaphorst, W. Van: A key role for iron-bound phosphorus in

871 authigenic apatite formation in North Atlantic continental platform sediments, J. Mar. Res., 54(6), 1179–1205,

872 doi:10.1357/0022240963213745, 1996b.

873 Slomp, C. P., Mort, H. P., Jilbert, T., Reed, D. C., Gustafsson, B. G. and Wolthers, M.: Coupled dynamics of iron

874 and phosphorus in sediments of an oligotrophic coastal basin and the impact of anaerobic oxidation of methane.,

875 PLoS One, 8(4), e62386, doi:10.1371/journal.pone.0062386, 2013.

876 Soetaert, K., Herman, P. M. J. and Middelburg, J. J.: A model of early diagenetic processes from the shelf to abyssal

877   depths, Geochim. Cosmochim. Acta, 60(6), 1019–1040, doi:10.1016/0016-7037(96)00013-0, 1996.

878   Soetaert, K. and Meysman, F.: Reactive transport in aquatic ecosystems: Rapid model prototyping in the open source

879   software R, Environ. Model. Softw., 32, 49–60, doi:10.1016/j.envsoft.2011.08.011, 2012.

880   Soetaert, K., Petzoldt, T. and Meysman, F. J. R.: marelac: Tools for Aquatic Sciences. R Package Version 2.1.3,

881   2010.

882   Soulet, G., Delaygue, G., Vallet-Coulomb, C., Böttcher, M. E., Sonzogni, C., Lericolais, G. and Bard, E.: Glacial

883   hydrologic conditions in the Black Sea reconstructed using geochemical pore water profiles, Earth Planet. Sci. Lett.,

884   296(1-2), 57–66, doi:10.1016/j.epsl.2010.04.045, 2010.

885   Soulet, G., Ménot, G., Lericolais, G. and Bard, E.: A revised calendar age for the last reconnection of the Black Sea

886   to the global ocean, Quat. Sci. Rev., 30(9-10), 1019–1026, doi:10.1016/j.quascirev.2011.03.001, 2011.

887   Stoll, M. H. C., Bakker, K., Nobbe, G. H. and Haese, R. R.: Continous-Flow Analysis of Dissolved Inorganic Carbon

888   Content in Seawater, Anal. Chem., 73(17), 4111–4116, doi:10.1021/ac010303r, 2001.

889   Strickland, J. D. and Parsons, T. R.: A Practical Handbook of Seawater Analysis, Bulletin 1., Fisheries Research

890   Board of Canada, Ottawa, Canada., 1972.

891   Suess, E.: Mineral phases formed in anoxic sediments by microbial decomposition of organic matter, Geochim.

892   Cosmochim. Acta, 43, 339–352, doi:10.1016/0016-7037(79)90199-6, 1979.

893   Thamdrup, B., Roselló-Mora, R. and Amann, R.: Microbial manganese and sulfate reduction in Black Sea shelf

894   sediments, Appl. Environ. Microbiol., 66(2251), 2288–2297, doi:10.1128/AEM.66.7.2888-2897.2000, 2000.

895   Treude, T., Krause, S., Maltby, J., Dale, A. W., Coffin, R. and Hamdan, L. J.: Sulfate reduction and methane

896   oxidation activity below the sulfate-methane transition zone in Alaskan Beaufort Sea continental margin sediments:

897   Implications for deep sulfur cycling, Geochim. Cosmochim. Acta, 144, 217–237, doi:10.1016/j.gca.2014.08.018,

898   2014.

899   Vargas, M., Kashefi, K., Blunt-Harris, E. L. and Lovley, D. R.: Microbial evidence for Fe(III) reduction on early

900   Earth, Nature, 395, 65–67, doi:10.1038/25720, 1998.

901   Wang, Y. and Van Cappellen, P.: A multicomponent reactive transport model of early diagenesis : Application to

902   redox cycling in coastal marine sediments, Geochim. Cosmochim. Acta, 60(16), 2993–3014, doi:10.1016/0016-

903   7037(96)00140-8, 1996.

904   Wankel, S. D., Adams, M. M., Johnston, D. T., Hansel, C. M., Joye, S. B. and Girguis, P. R.: Anaerobic methane

905   oxidation in metalliferous hydrothermal sediments: influence on carbon flux and decoupling from sulfate reduction,

906   Environ. Microbiol., 14(10), 2726–40, doi:10.1111/j.1462-2920.2012.02825.x, 2012.

907   Whiticar, M. J.: Carbon and hydrogen isotope systematics of bacterial formation and oxidation of methane, Chem.

908   Geol., 161(1-3), 291–314, doi:10.1016/S0009-2541(99)00092-3, 1999.

909   Yoshinaga, M. Y., Holler, T., Goldhammer, T., Wegener, G., Pohlman, J. W., Brunner, B., Kuypers, M. M. M.,

910   Hinrichs, K. and Elvert, M.: Carbon isotope equilibration during sulphate-limited anaerobic oxidation of methane,

911   Nat. Geosci., 7, 190–194, doi:10.1038/NGEO2069, 2014.

912   Zhou, S., Xu, J., Yang, G. and Zhuang, L.: Methanogenesis affected by the co-occurrence of iron(III) oxides and

913   humic substances, FEMS Microbiol. Ecol., 88(1), 107–120, doi:10.1111/1574-6941.12274, 2014.

914   Zhuang, L., Xu, J., Tang, J. and Zhou, S.: Effect of ferrihydrite biomineralization on methanogenesis in an anaerobic

915   incubation from paddy soil, J. Geophys. Res. Biogeosciences, (120), 876–886, doi:10.1002/2014JG002893, 2015.

916

917

Tables

919   **Table 1. Overview of the sequential P, Fe and S fractionation methods used in this study.**

Step and code	Extractant, extraction time	Target phase
P fractionation (modified from Ruttenberg (1992); done for site 4 (MC & GC) and site 5 (MC & GC))		
1 P_{exch}	1 M $MgCl_2$, pH 8, 0.5 h	Exchangeable P
2[a] P_{Fe}	25 g L-1 Na dithionite, pH 7.5, 8 h	Fe-associated P
3[a] $P_{authi\ Ca-P}$	Na acetate buffer, pH 4, 6 h	P in authigenic and biogenic Ca-P minerals and $CaCO_3$
4 P_{detr}	1 M HCl, 24 h	Detrital P
5 P_{org}	Ashing at 550 °C (2h), then 1 M HCl, 24 h	Organic P
Fe fractionation (after Poulton and Canfield (2005); done for site 4 (MC & GC) and site 5 (MC))		
1 Fe_{carb}	1 M Na acetate, pH 4.5, 24 h	Carbonate-associated Fe
2 Fe_{ox1}	1 M hydroxylamine-HCl, 24 h	Amorphous Fe oxides (ferrihydrite)
3 Fe_{ox2}	50 g L-1 Na dithionite, pH 4.8, 2 h	Crystalline Fe oxides (goethite, hematite)
4 Fe_{mag}	0.2 M ammonium oxalate/ 0.17 M oxalic acid, 2 h	Recalcitrant Fe oxides (mostly magnetite)
Fe fractionation (modified from Claff et al. (2010); done for site 4 (MC & GC) and site 5 (MC))		
1 $Fe(II)_{HCl}$	1 M HCl, 4 h	Labile Fe (carbonates, poorly ordered sulfides)
2 $Fe(III)_{HCl}$	1 M HCl, 4 h	Labile Fe (easily reducible oxides)
3 $Fe(III)_{CDB}$	50 g L-1 Na dithionite, pH 4.8, 4 h	Crystalline Fe oxides
4 Fe_{pyrite}	Concentrated HNO_3, 2 h	Pyrite (FeS_2)
S fractionation (after Burton et al. (2008); done for site 4 (MC) and site 5 (MC & GC))		
1 AVS	6 M HCl, 24 h	S in Fe monosulfides (FeS)
2 CRS	Acidic chromous chloride solution, 48 h	S in pyrite (FeS_2)

920   [a]These steps were followed by a wash step with 1 M $MgCl_2$, which was added to the corresponding step. MC = multicore and GC

921   = gravity core.

922

923 **Table 2. Chemical species included in the diagenetic model.**

Species	Notation	Type
Organic matter[a]	$OM^{\alpha,\beta,\gamma}$	Solid
Iron oxides[a]	$Fe(OH)_3^{\alpha,\beta,\gamma}$	Solid
Iron monosulfide	FeS	Solid
Pyrite	FeS_2	Solid
Siderite	$FeCO_3$	Solid
Elemental sulfur	S_0	Solid
Iron oxide-bound phosphorus	$Fe_{ox}P$	Solid
Vivianite	$Fe_3(PO_4)_2$	Solid
Organic phosphorus	P_{org}	Solid
Authigenic (Ca) phosphorus	CaP	Solid
Detrital phosphorus	$DetrP$	Solid
Chloride	Cl^-	Solute
Oxygen	O_2	Solute
Sulfate	SO_4^{2-}	Solute
Iron	Fe^{2+}	Solute
Hydrogen sulfide[b]	$\sum H_2S$	Solute
Methane	CH_4	Solute
Ammonium[b]	$\sum NH_4^+$	Solute
Nitrate	NO_3^-	Solute
Phosphate	$\sum HPO_4^{2-}$	Solute
Dissolved inorganic carbon	DIC	Solute

924   [a] There are three types of species: reactive (α), less reactive (β) and refractory (γ)

925   [b] $\sum$ denotes that all species of an acid are included

926

Table 3. Reaction pathways and stoichiometries implemented in the diagenetic model.

Primary redox reactions*	
$OM^{\alpha,\beta} + aO_2 \rightarrow aCO_2 + bNH_4^+ + cH_3PO_4 + aH_2O$	R1
$OM^{\alpha,\beta} + \frac{4a}{5}NO_3^- + \frac{4a}{5}H^+ \rightarrow aCO_2 + bNH_4^+ + cH_3PO_4 + \frac{2a}{5}N_2 + \frac{7a}{5}H_2O$	R2
$OM^{\alpha,\beta} + 4aFe(OH)_3^\alpha + 4a\chi^\alpha Fe_{ox}P + 12aH^+ \rightarrow aCO_2 + bNH_4^+ + (c + 4a\chi^\alpha)H_3PO_4 + 4aFe^{2+} + 13aH_2O$	R3
$OM^{\alpha,\beta} + \frac{a}{2}SO_4^{2-} + aH^+ \rightarrow aCO_2 + bNH_4^+ + cH_3PO_4 + \frac{a}{2}H_2S + aH_2O$	R4
$OM^{\alpha,\beta} \rightarrow \frac{a}{2}CO_2 + bNH_4^+ + cH_3PO_4 + \frac{a}{2}CH_4$	R5
$CO_2 + 4H_2 \rightarrow CH_4 + 2H_2O$	R6

Secondary redox and other reaction equations[†]	
$2O_2 + NH_4^+ + 2HCO_3^- \rightarrow NO_3^- + 2CO_2 + 3H_2O$	R7
$O_2 + 4Fe^{2+} + 8HCO_3^- + 2H_2O + 4\chi^\alpha H_2PO_4^- \rightarrow 4Fe(OH)_3^\alpha + 4\chi^\alpha Fe_{ox}P + 8CO_2$	R8
$2O_2 + FeS \rightarrow SO_4^{2-} + Fe^{2+}$	R9
$7O_2 + 2FeS_2 + 2H_2O \rightarrow 4SO_4^{2-} + 2Fe^{2+} + 4H^+$	R10
$2O_2 + H_2S + 2HCO_3^- \rightarrow SO_4^{2-} + 2CO_2 + 2H_2O$	R11
$2O_2 + CH_4 \rightarrow CO_2 + 2H_2O$	R12
$2Fe(OH)_3^\alpha + 2\chi^\alpha Fe_{ox}P + H_2S + 4CO_2 \rightarrow 2Fe^{2+} + 2\chi^\alpha H_2PO_4^- + S_0 + 4HCO_3^- + 2H_2O$	R13
$2Fe(OH)_3^\beta + 2\chi^\beta Fe_{ox}P + H_2S + 4CO_2 \rightarrow 2Fe^{2+} + 2\chi^\beta H_2PO_4^- + S_0 + 4HCO_3^- + 2H_2O$	R14
$Fe^{2+} + H_2S \rightarrow FeS + 2H^+$	R15
$FeS + H_2S \rightarrow FeS_2 + H_2$	R16
$4S_0 + 4H_2O \rightarrow 3H_2S + SO_4^{2-} + 2H^+$	R17
$FeS + S_0 \rightarrow FeS_2$	R18
$SO_4^{2-} + CH_4 + CO_2 \rightarrow 2HCO_3^- + H_2S$	R19
$CH_4 + 8Fe(OH)_3^{\alpha,\beta} + 8\chi^{\alpha,\beta}Fe_{ox}P + 15H^+ \rightarrow HCO_3^- + 8Fe^{2+} + 8\chi^{\alpha,\beta}H_2PO_4^- + 21H_2O$	R20
$Fe(OH)_3^\alpha + (\chi^\alpha - \chi^\beta)Fe_{ox}P \rightarrow Fe(OH)_3^\beta + (\chi^\alpha - \chi^\beta)H_2PO_4^-$	R21
$Fe(OH)_3^\beta + (\chi^\beta - \chi^\gamma)Fe_{ox}P \rightarrow Fe(OH)_3^\gamma + (\chi^\beta - \chi^\gamma)H_2PO_4^-$	R22
$3Fe^{2+} + 2HPO_4^{2-} \rightarrow Fe_3(PO_4)_2 + 2H^+$	R23
$Fe^{2+} + CO_3^{2-} \rightarrow FeCO_3$	R24
$FeCO_3 + H_2S \rightarrow FeS + HCO_3^- + H^+$	R25
$Fe_3(PO_4)_2 + 3H_2S \rightarrow 3FeS + 2HPO_4^{2-} + 4H^+$	R26

928 * Organic matter (OM) is of the form $(CH_2O)_a(NH_4^+)_b(H_3PO_4)_c$, with 'a'=1, 'b' = 1/16 and 'c' = 1/106. Under anoxic bottom
929 water conditions, 'c' reduces to 0.25 to account for the preferential regeneration of P (e.g. Ingall et al. (1993)). † $\chi^{\alpha,\beta,\gamma}$ refers to
930 the P:Fe ratio of $Fe(OH)_3^{\alpha,\beta,\gamma}$ (see Supplementary Table S1). *R6* = CH_4 production from DIC (i.e. CO_2); *R7* = nitrification; *R8* =
931 $Fe(OH)_3$ formation; *R9* = FeS oxidation; *R10* = FeS_2 oxidation; *R11* = H_2S oxidation; *R12* = aerobic CH_4 oxidation; *R13* and *R14*
932 = $Fe(OH)_3$ reduction by H_2S; *R15*= FeS formation; *R16* = pyrite formation (H_2S pathway); *R17* = S_0 disproportionation; *R18* =
933 pyrite formation (polysulfide pathway); *R19* = SO_4-AOM; *R20* = Fe-AOM; *R21* = conversion (i.e. crystallization) from α to β
934 phase; *R22* = crystallization from β to γ phase; *R23* = vivianite formation; *R24* = siderite precipitation; *R25* = conversion from
935 siderite to FeS; *R26* = vivianite dissolution by dissolved sulfide
936
937

938   **Table 4. Reaction equations implemented in the model.**

Primary redox reaction equations

$$R_1 = k_{\propto,\beta} OM^{\propto,\beta} \left(\frac{[O_2]}{K_{O_2}+[O_2]} \right)$$ (E1)

$$R_2 = k_{\propto,\beta} OM^{\propto,\beta} \left(\frac{[NO_3^-]}{K_{NO_3^-}+[NO_3^-]} \right) \left(\frac{K_{O_2}}{K_{O_2}+[O_2]} \right)$$ (E2)

$$R_3 = k_{\propto,\beta} OM^{\propto,\beta} \left(\frac{[Fe(OH)_3^\alpha]}{K_{Fe(OH)_3^\alpha}+[Fe(OH)_3^\alpha]} \right) \left(\frac{K_{NO_3^-}}{K_{NO_3^-}+[NO_3^-]} \right) \left(\frac{K_{O_2}}{K_{O_2}+[O_2]} \right)$$ (E3)

$$R_4 = \Psi k_{\propto,\beta} OM^{\propto,\beta} \left(\frac{[SO_4^{2-}]}{K_{SO_4^{2-}}+[SO_4^{2-}]} \right) \left(\frac{K_{Fe(OH)_3^\alpha}}{K_{Fe(OH)_3^\alpha}+[Fe(OH)_3^\alpha]} \right) \left(\frac{K_{NO_3^-}}{K_{NO_3^-}+[NO_3^-]} \right) \left(\frac{K_{O_2}}{K_{O_2}+[O_2]} \right)$$ (E4)

$$R_5 = \Psi k_{\propto,\beta} OM^{\propto,\beta} \left(\frac{K_{SO_4^{2-}}}{K_{SO_4^{2-}}+[SO_4^{2-}]} \right) \left(\frac{K_{Fe(OH)_3^\alpha}}{K_{Fe(OH)_3^\alpha}+[Fe(OH)_3^\alpha]} \right) \left(\frac{K_{NO_3^-}}{K_{NO_3^-}+[NO_3^-]} \right) \left(\frac{K_{O_2}}{K_{O_2}+[O_2]} \right)$$ (E5)

$$R_6 = k_1 DIC \left(\frac{K_{SO_4^{2-}}}{K_{SO_4^{2-}}+[SO_4^{2-}]} \right) \left(\frac{K_{Fe(OH)_3^\alpha}}{K_{Fe(OH)_3^\alpha}+[Fe(OH)_3^\alpha]} \right) \left(\frac{K_{NO_3^-}}{K_{NO_3^-}+[NO_3^-]} \right) \left(\frac{K_{O_2}}{K_{O_2}+[O_2]} \right)$$ (E6)

Secondary redox and other reaction equations

$$R_7 = k_2[O_2][NH_4^+]$$ (E7)

$$R_8 = k_3[O_2][Fe^{2+}]$$ (E8)

$$R_9 = k_4[O_2][FeS]$$ (E9)

$$R_{10} = k_5[O_2][FeS_2]$$ (E10)

$$R_{11} = k_6[O_2][\sum H_2S]$$ (E11)

$$R_{12} = k_7[O_2][CH_4]$$ (E12)

$$R_{13} = k_8[Fe(OH)_3^\propto][\sum H_2S]$$ (E13)

$$R_{14} = k_9[Fe(OH)_3^\beta][\sum H_2S]$$ (E14)

$$R_{15} = k_{10}[Fe^{2+}][\sum H_2S]$$ (E15)

$$R_{16} = k_{11}[FeS][\sum H_2S]$$ (E16)

$$R_{17} = k_{12}[S_0]$$ (E17)

$$R_{18} = k_{13}[FeS][S_0]$$ (E18)

$$R_{19} = k_{14}[SO_4^{2-}][CH_4]$$ (E19)

$$R_{20} = k_{15}[Fe(OH)_3^{\propto,\beta}][CH_4]$$ (E20)

$$R_{21} = k_{16}[Fe(OH)_3^\propto]$$ (E21)

$$R_{22} = k_{17}[Fe(OH)_3^\beta]$$ (E22)

$$R_{23} = k_{18}[Fe^{2+}][HPO_4^{2-}]$$ (E23)

$$R_{24} = k_{19}[Fe^{2+}][DIC]$$ (E24)

$$R_{25} = k_{20}[FeCO_3][\sum H_2S]$$ (E25)

$$R_{26} = k_{21}[Fe_3(PO_4)_2][\sum H_2S]$$ (E26)

939

940

Table 5. Reaction parameters used in the diagenetic model.

Parameter	Symbol	Value	Units	Values given in literature
Decay constant for OM$^\alpha$	k_α	0.05	yr^{-1}	0.05-1.62[a,b]
Decay constant for OM$^\beta$	k_β	0.0086	yr^{-1}	0.0086[b]
Limiting concentration of O_2	K_{O2}	0.02	mM	0.001-0.03[c]
Limiting concentration of NO_3^-	K_{NO3-}	0.004	mM	0.004-0.08[c]
Limiting concentration of $Fe(OH)_3$	$K_{Fe(OH)3}$	65	μmol g^{-1}	65-100[c]
Limiting concentration of SO_4^{2-}	K_{SO42-}	1.6	mM	1.6[c]
Attenuation factor for SO_4^{2-} and methanogenesis	Ψ	0.0042	-	0.00157-0.075[b,d]
Rate constant for reaction *E6*	k_1	0.0011	yr^{-1}	
Rate constant for reaction *E7*	k_2	10'000	mM^{-1} yr^{-1}	5'000-39'000[c,d]
Rate constant for reaction *E8*	k_3	140'000	mM^{-1} yr^{-1}	140'000[c]
Rate constant for reaction *E9*	k_4	300	mM^{-1} yr^{-1}	300[c]
Rate constant for reaction *E10*	k_5	1	mM^{-1} yr^{-1}	1[c]
Rate constant for reaction *E11*	k_6	160	mM^{-1} yr^{-1}	$\geq$ 160[c]
Rate constant for reaction *E12*	k_7	10'000'000	mM^{-1} yr^{-1}	10'000'000[c]
Rate constant for reaction *E13*	k_8	9.5	mM^{-1} yr^{-1}	$\leq$ 100[c]
Rate constant for reaction *E14*	k_9	0.95	mM^{-1} yr^{-1}	Model constrained
Rate constant for reaction *E15*	k_{10}	150	mM^{-1} yr^{-1}	100-14'800[b, d]
Rate constant for reaction *E16*	k_{11}	0.0003	mM^{-1} yr^{-1}	3.15[e]
Rate constant for reaction *E17*	k_{12}	3	yr^{-1}	3[f]
Rate constant for reaction *E18*	k_{13}	1	mM^{-1} yr^{-1}	7[f]
Rate constant for reaction *E19*	k_{14}	0.14	mM^{-1} yr^{-1}	10[c]
Rate constant for reaction *E20*	k_{15}	0.00000016	mM^{-1} yr^{-1}	0.0074[g]
Rate constant for reaction *E21*	k_{16}	0.6	yr^{-1}	0.6[f]
Rate constant for reaction *E22*	k_{17}	0.000013	yr^{-1}	Model constrained
Rate constant for reaction *E23*	k_{18}	0.052	mM^{-1} yr^{-1}	Model constrained
Rate constant for reaction *E24*	k_{19}	0.0027	mM^{-1} yr^{-1}	Model constrained
Rate constant for reaction *E25*	k_{20}	0.0008	mM^{-1} yr^{-1}	Model constrained
Rate constant for reaction *E26*	k_{21}	0.0008	mM^{-1} yr^{-1}	Model constrained

942   [a] Moodley et al. (2005); [b] Reed et al. (2011a); [c] Wang and Van Cappellen (1996); [d] Reed et al. (2011b); [e] Rickard and Luther

943   (1997); [f] Berg et al. (2003); [g] Rooze et al. (2016)

944

945

946

947　**Table 6. Depth-integrated rates of key processes for selected depth intervals in µmol m^{-2} d^{-1}.**

Process	0 – 90 cm[a]	90 - 300 cm[b]	300 – 800 cm[c]	0 – 800 cm
Organoclastic SO$_4^{2-}$ reduction[d]	68.9	5.3	0.003	74.2
CH$_4$ production[e,f]	10.21	37.7	91.8	139.8
SO$_4$ - AOM	9.4	151.6	1.2	162.2
Fe – AOM[e]	0	0	1.2	1.2
S$_0$ disproportionation	0	0	0.9	0.9

948　[a] Marine deposits ; [b] limnic sediments around the SMTZ with dissolved sulfide; [c] non-sulfidic limnic deposits; [d] per mol of SO$_4^{2-}$; [e]

949　per mol of CH$_4$; [f] sum of CH$_4$ production from organic matter and from DIC (i.e. CO$_2$)

950

951

952

33
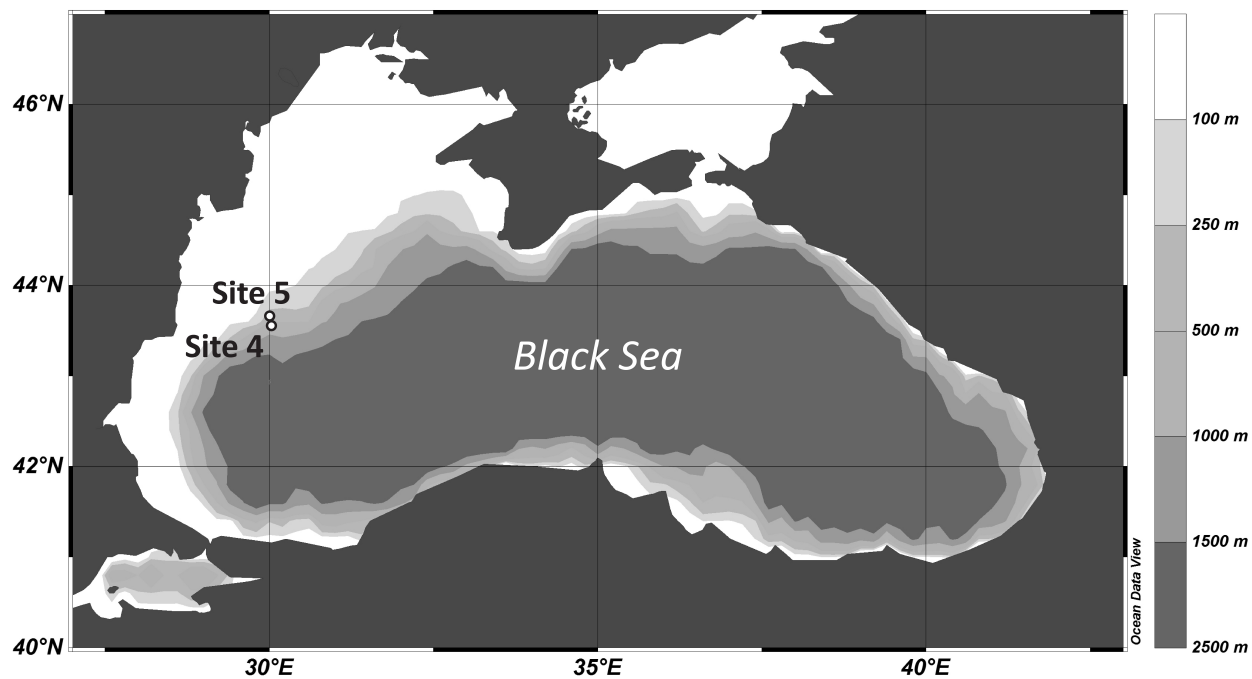
Figures

Figure 1. Map showing the locations of site 4 (43°40.6' N, 30°7.5' E; 377 mbss) and site 5 (43°42.6' N, 30°6.1' E; 178 mbss), sampled in June 2013.

957

958

34
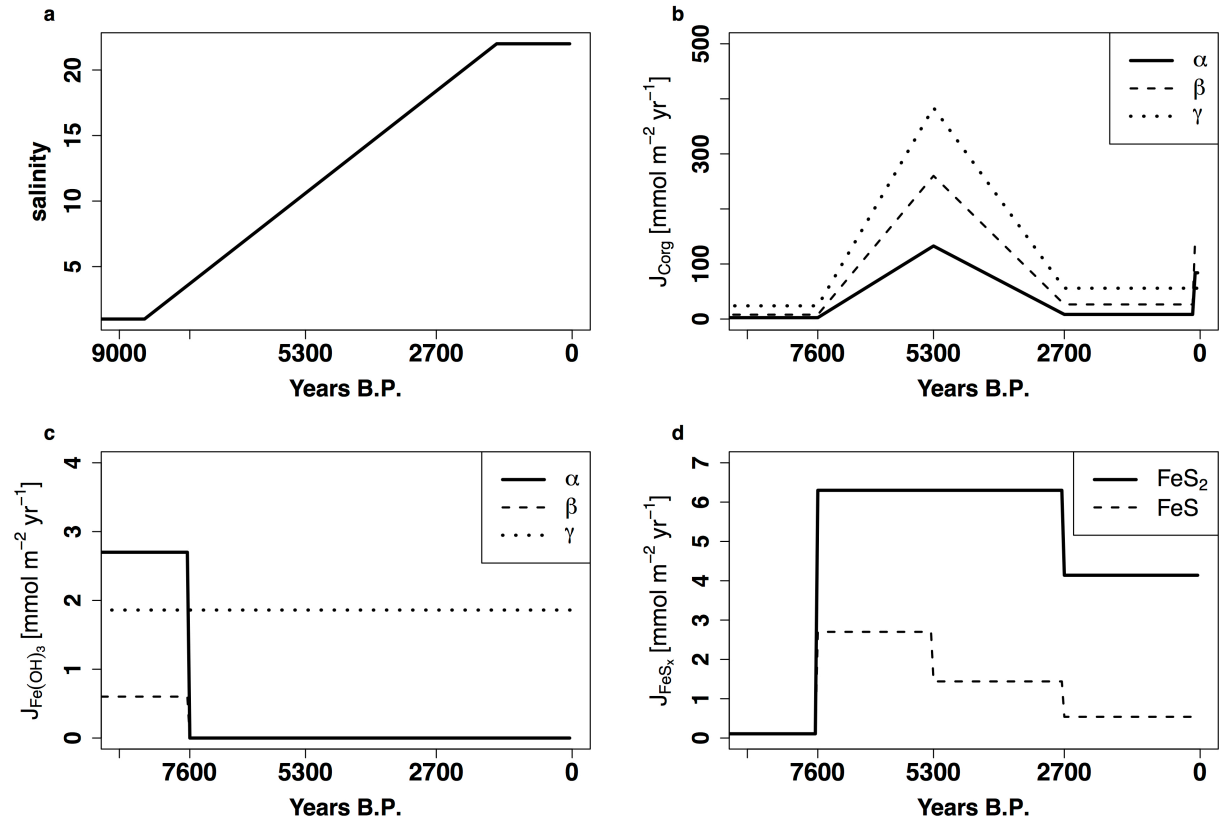
959

960   **Figure 2. Transient evolution of salinity with a linear increase from 1 to 22 between 8500 and 1500 years B.P. (a), fluxes of**
961   **organic matter ($J_{C_{Org}}$; b), Fe oxides ($J_{Fe(OH)_3}$; c) and Fe sulfides (J_{FeS_x}; d) as implemented in the diagenetic model (site 4).**

962

35

963
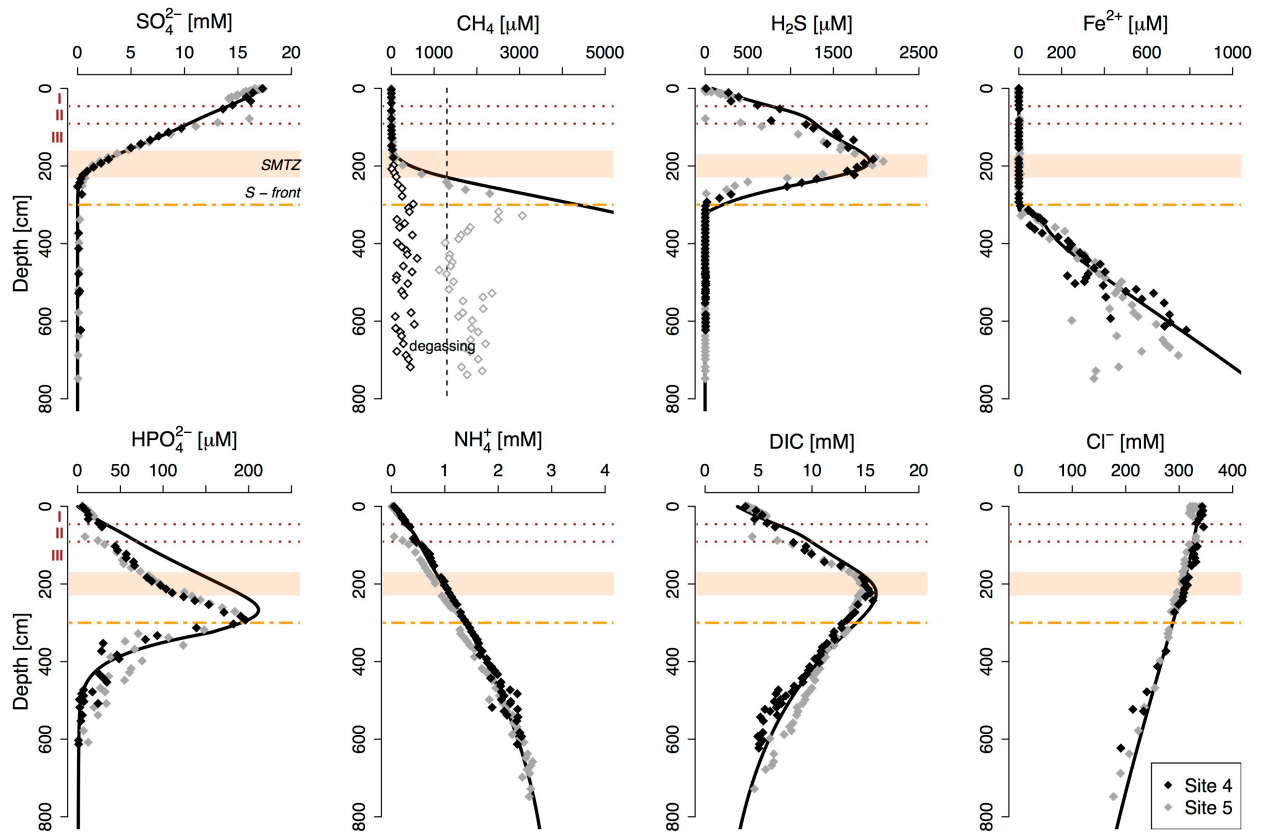
Figure 3. Pore water profiles of key components for site 4 (black diamonds) and site 5 (gray diamonds) and corresponding modeled profiles as calculated with the diagenetic model (black lines). Red dotted lines and roman numbers indicate the transitions between the lithological Unit I (modern coccolith ooze), Unit II (marine sapropel) and Unit III (limnic deposits). The orange bar represents the sulfate-methane transition zone (SMTZ) and the orange dashed line shows the current position of the downward migrating sulfidization front (S-front). The dashed vertical line indicates the CH_4 saturation concentration at atmospheric pressure (Mogollón et al., 2013). The open diamonds indicate CH_4 concentrations that are likely underestimated due to outgassing of CH_4 during coring.

971

972
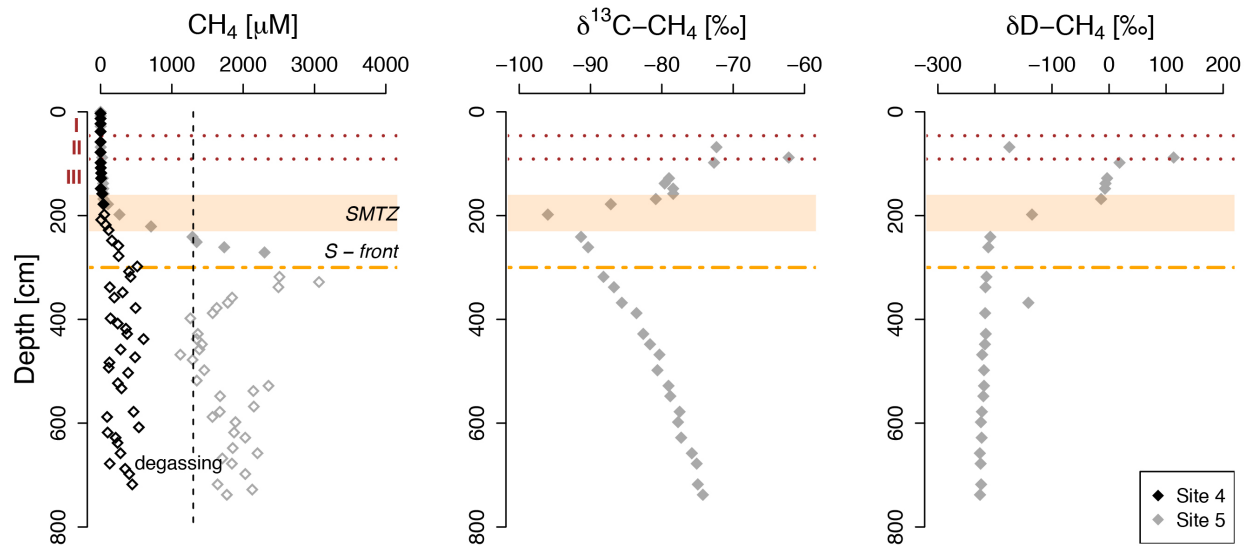
973

974 **Figure 4. Pore water profiles of CH$_4$ for site 4 (black diamonds) and 5 (gray diamonds) and corresponding isotopic**

975 **composition of dissolved CH$_4$ (available for site 5 only). δ^{13}C-CH$_4$ values are given in ‰ vs. VPDB (Vienna Pee Dee**

976 **Belemnite) and δD-CH$_4$ values are given in ‰ vs. V-SMOW (Vienna Standard Mean Ocean Water). Red dotted lines and**

977 **roman numbers indicate the transitions between the lithological Unit I (modern coccolith ooze), Unit II (marine sapropel)**

978 **and Unit III (limnic deposits). The orange bar represents the sulfate-methane transition zone (SMTZ) and the orange**

979 **dashed line shows the current position of the downward migrating sulfidization front (S-front). The dashed vertical line**

980 **indicates the CH$_4$ saturation concentration at atmospheric pressure (Mogollón et al., 2013). The open diamonds indicate**

981 **CH$_4$ concentrations that are likely underestimated due to outgassing of CH$_4$ during coring.**

982
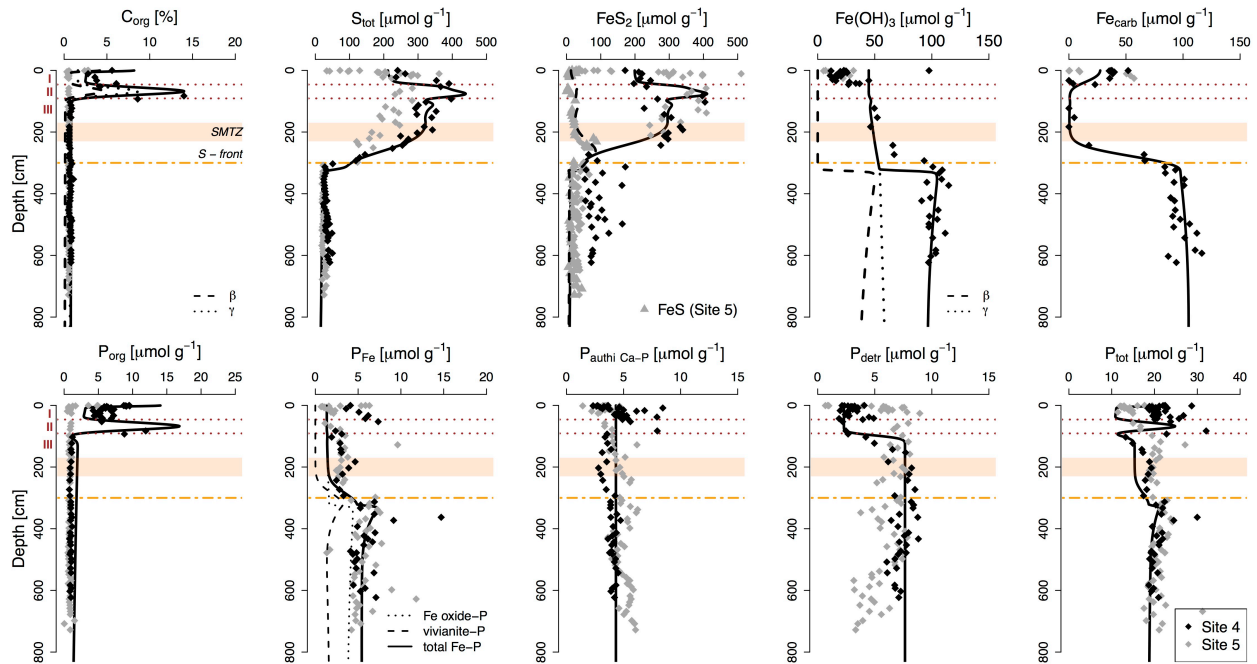
983

984 **Figure 5. Solid phase sediment profiles for site 4 (black diamonds) and 5 (gray diamonds). Fe oxides represent the sum of**

985 **amorphous, crystalline and recalcitrant oxides, i.e. Fe_{ox1}, Fe_{Ox2} and Fe_{mag} (Table 1, Supplementary Fig. S4). Fe_{carb} was**

986 **corrected for apparent AVS dissolution during the Na acetate extraction step (the uncorrected Fe_{carb} data is given in**

987 **Supplementary Fig. S4). Black lines represent profiles derived from the diagenetic model. Red dotted lines and roman**

988 **numbers indicate the transitions between the lithological Unit I (modern coccolith ooze), Unit II (marine sapropel) and**

989 **Unit III (limnic deposits). The orange bar represents the sulfate-methane transition zone (SMTZ) and the orange dashed**

990 **line shows the current position of the downward migrating sulfidization front (S-front).**

991

38
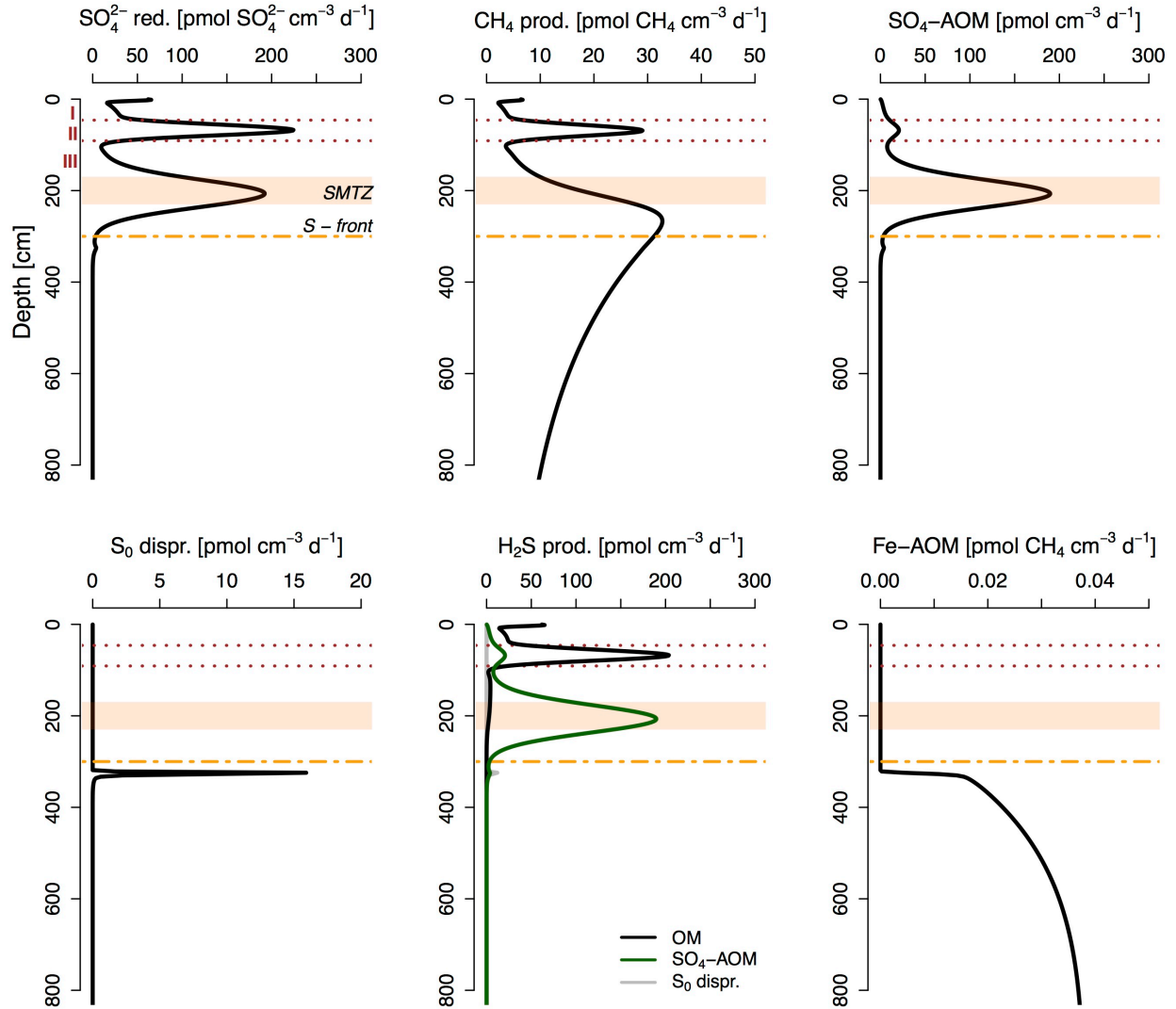
Figure 6. Modeled rates of total SO_4^{2-} reduction, total CH_4 production, SO_4-AOM, S_0 disproportionation, sulfide production and Fe-AOM. Red dotted lines and roman numbers indicate the transitions between the lithological Unit I (modern coccolith ooze), Unit II (marine sapropel) and Unit III (limnic deposits). The orange bar represents the sulfate-methane transition zone (SMTZ) and the orange dashed line shows the current position of the downward migrating sulfidization front (S-front).

39

999
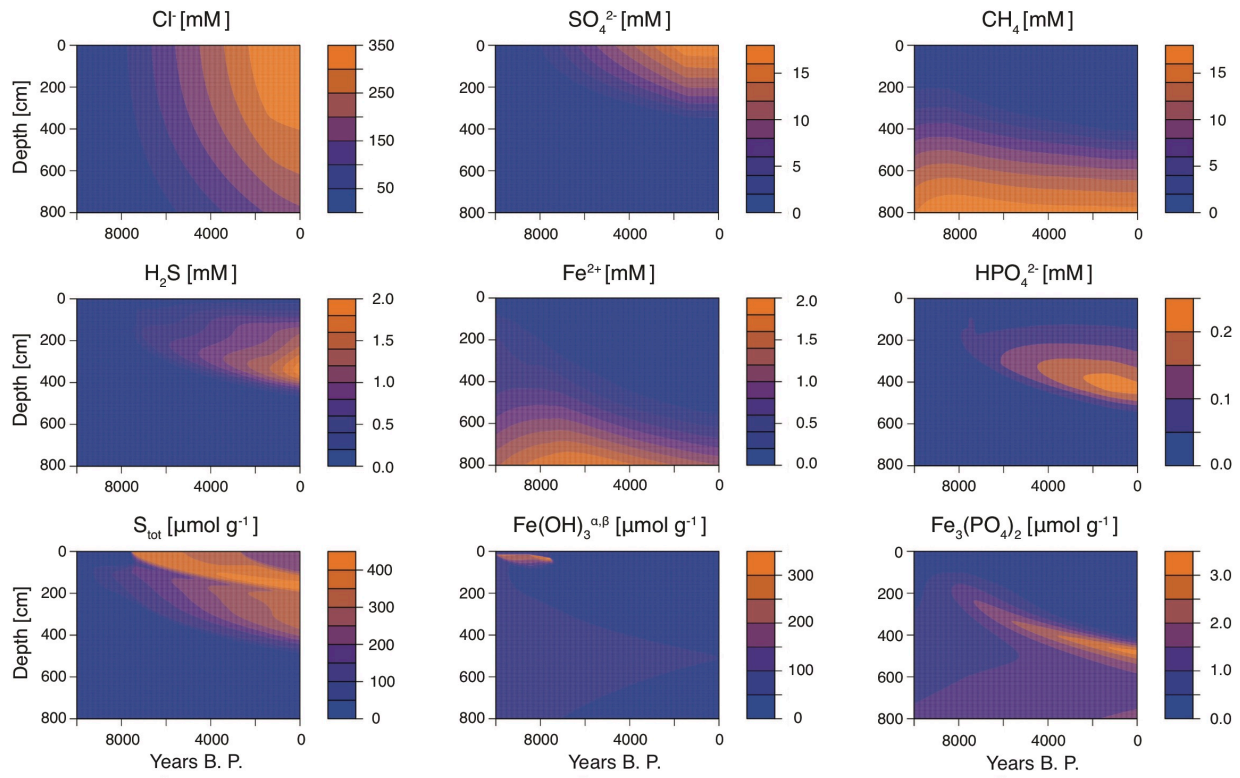
Figure 7. Transient evolution of selected pore water and sediment profiles with depth as calculated for site 4 using the diagenetic model.

1002

1003
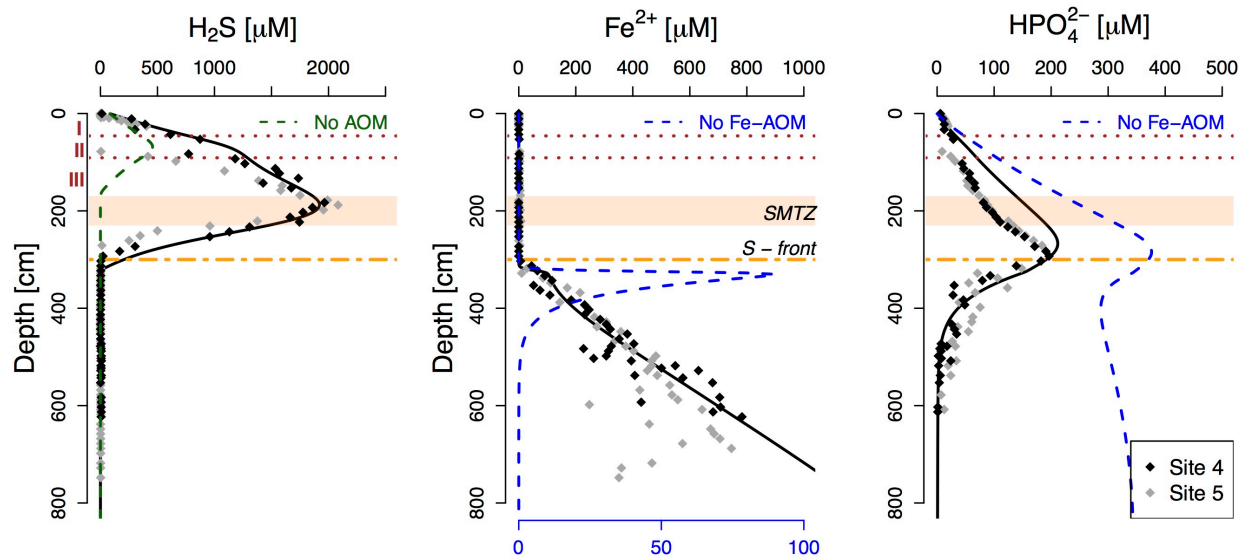

1004

1005 **Figure 8. Pore water profiles of dissolved sulfide, Fe^{2+} and HPO_4^{2-}. The green dashed line represents the modeled sulfide**

1006 **profile without SO_4-AOM, indicating that the latter significantly enhances the downward sulfidization. Blue dashed lines**

1007 **denote the modeled Fe^{2+} and HPO_4^{2-} profiles without ongoing Fe oxide reduction in the limnic deposits (i.e. no Fe-AOM).**

1008 **Note that concentrations of Fe^{2+} were multiplied 10 times in the model simulation without Fe oxide reduction to better**

1009 **visualize the potential release of Fe^{2+} through a cryptic S cycle (corresponding x axis at bottom). Red dotted lines and**

1010 **roman numbers indicate the transitions between the lithological Unit I (modern coccolith ooze), Unit II (marine sapropel)**

1011 **and Unit III (limnic deposits). The orange bar represents the sulfate-methane transition zone (SMTZ) and the orange**

1012 **dashed line shows the current position of the downward migrating sulfidization front (S-front).**

1013
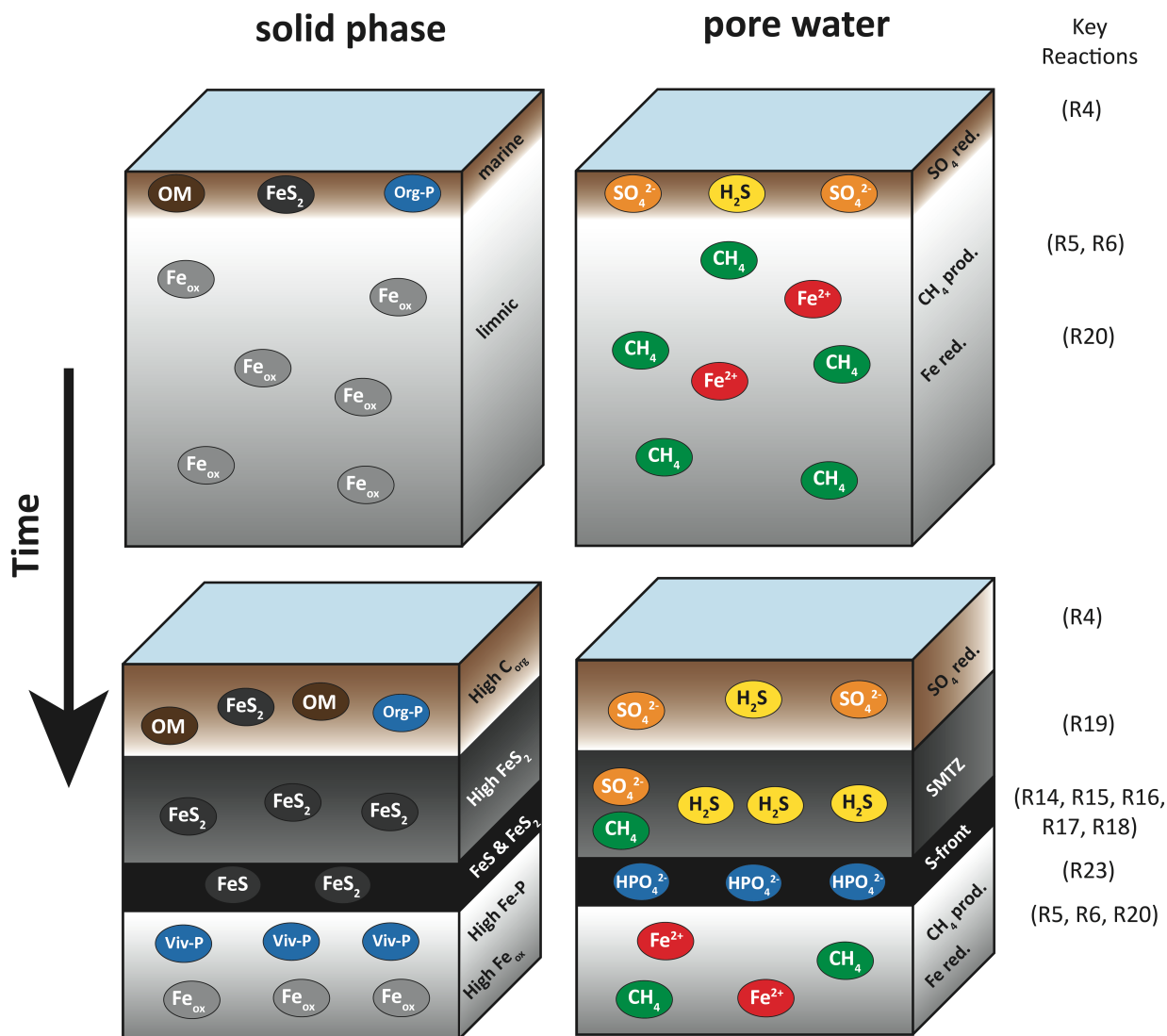
Figure 9. Schematic of the main diagenetic processes discussed in this study and their imprint on the geochemical solid phase (left) and pore water profiles (right). Accumulation of marine sediments with time and the subsequent downward diffusion of SO_4^{2-} into the CH_4-bearing limnic sediment stimulate SO_4-AOM around the sulfate-methane transition zone (SMTZ), thus enhancing the downward sulfidization of the Fe oxide-rich lake deposits. Below the sulfidization front (S-front), HPO_4^{2-} released during reductive dissolution of Fe oxides is bound again in vivianite, leading to an enrichment in sedimentary P in these sediments. Numbers on the right indicate the key reactions occurring in the corresponding sediment layers as described in Table 3. Note that in this study, Fe-AOM (R20) was assumed as the main source of pore water Fe^{2+} below the S-front to further test the potential impact of Fe-AOM on pore water CH_4. However, based on the geochemical data, we cannot exclude a potential role for organoclastic Fe reduction (R3) and/or reactivation of less reactive Fe oxides by methanogens.